JCI The Journal of Clinical Investigation

Aggressive B-cell lymphomas retain ATR-dependent determinants of T-cell exclusion from the Germinal Center Dark Zone

Valeria Cancila, … , Anand D. Jeyasekharan, Claudio Tripodo

J Clin Invest. 2025. https://doi.org/10.1172/JCI187371.

Research In-Press Preview Cell biology Immunology Oncology

Graphical abstract

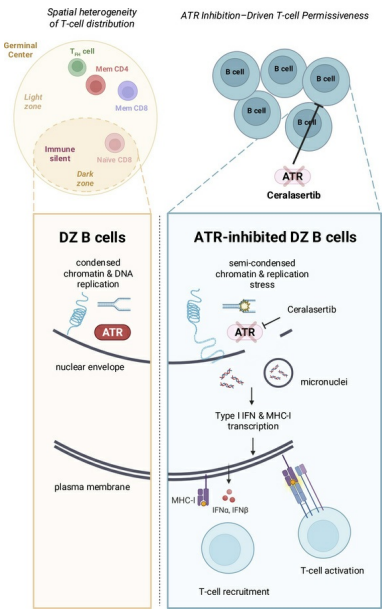

Find the latest version:

https://jci.me/187371/pdf

Aggressive B-cell lymphomas retain ATR-dependent determinants of T-cell exclusion from the Germinal Center Dark Zone

Valeria Cancila[1§], Giorgio Bertolazzi[2§], Allison S. Y. Chan[3§], Giovanni Medico[1,4], Giulia Bastianello[5], Gaia Morello[1], Daniel Paysan[6,7], Clemence Lai[3], Hong Liang[3], Girija Shenoy[3], Patrick W. Jaynes[3], Giovanna Schiavoni[8], Fabrizio Mattei[8], Silvia Piconese[9,10,11], Maria V. Revuelta[12], Francesco Noto[8], Luca Businaro[13], Adele De Ninno[13], Ilenia Cammarata[14], Fabio Pagni[15], Saradha Venkatachalapathy[6,7], Sabina Sangaletti[16], Arianna Di Napoli[17], Giada Cicio[18], Davide Vacca[1], Silvia Lonardi[19], Luisa Lorenzi[19], Andrés J. M. Ferreri[20,21], Beatrice Belmonte[1], Min Liu[3,22-23], Manikandan Lakshmanan[24], Michelle S. N. Ong[24], Zhang Biyan[25], Tingyi See[25], Kong-Peng Lam[25-27], Gabriele Varano[28], Mario P. Colombo[16], Silvio Bicciato[29], Giorgio Inghirami[4], Leandro Cerchietti[12], Maurilio Ponzoni[21,30], Roberta Zappasodi[31], Evelyn Metzger[32], Joe Beechem[32], Fabio Facchetti[19], Marco Foiani[5], Stefano Casola[28, 33§], Anand D. Jeyasekharan[3,34-36§], Claudio Tripodo[1,18, 37§*].

[1] Tumor Immunology Unit, Department of Health Sciences, University of Palermo, Palermo, Italy
[2] Department of Medicine and Surgery, Kore University of Enna, Enna, Italy
[3] Cancer Science Institute of Singapore, National University of Singapore, Republic of Singapore
[4] Division of Hematopathology, Department of Pathology and Laboratory Medicine, Weill Cornell Medicine/NewYork-Presbyterian Hospital, New York
[5] Genome Integrity Lab, IFOM ETS-The AIRC Institute of Molecular Oncology, Milan, Italy
[6] Laboratory for Nanoscale Biology, Paul Scherrer Institute, Villigen, Switzerland
[7] Department of Health Sciences and Technology, ETH Zurich, Zurich, Switzerland
[8] Department of Oncology and Molecular Medicine, Istituto Superiore di Sanità, Rome, Italy
[9] Department of Internal Clinical Sciences, Anesthesiology and Cardiovascular Sciences, Sapienza University of Rome, Rome, Italy
[10] IRCCS Fondazione Santa Lucia, Unità di Neuroimmunologia, Rome, Italy
[11] Laboratory affiliated to Istituto Pasteur Italia-Fondazione Cenci Bolognetti, Rome, Italy
[12] Division of Hematology and Oncology, Medicine Department, Weill Cornell Medicine and NewYork-Presbyterian Hospital, New York
[13] Institute for Photonics and Nanotechnologies, Italian National Research Council, Rome, Italy
[14] Department of Translational and Precision Medicine, Sapienza University of Rome, Rome, Italy; Neuroimmunology Unit, IRCCS Fondazione Santa Lucia, Rome, Italy
[15] Department of Medicine and Surgery, Pathology, IRCCS Fondazione San Gerardo dei Tintori, University of Milano-Bicocca, Milan, Italy
[16] Molecular Immunology Unit, Department of Experimental Oncology, Fondazione IRCCS Istituto Nazionale Tumori, Milan, Italy
[17] Pathology Unit, Department of Clinical and Molecular Medicine, Sant'Andrea University Hospital, Sapienza University of Rome, Rome, Italy
[18] Advanced Pathology Laboratory, IFOM ETS-The AIRC Institute of Molecular Oncology, Milan, Italy

[19] Pathology Unit, ASST Spedali Civili di Brescia, Department of Molecular and Translational Medicine, University of Brescia, Brescia, Italy
[20] Lymphoma Unit, IRCCS San Raffaele Scientific Institute, Milan, Italy
[21] Vita-Salute San Raffaele University, Milan, Italy
[22] Department of Radiation Oncology, Chongqing University Cancer Hospital, Chongqing, PR China
[23] Department of Immunology, Tianjin Medical University Cancer Institute and Hospital, Tianjin, PR China
[24] Institute of Molecular and Cell Biology (IMCB), Agency for Science, Technology and Research (A*STAR), Singapore, Republic of Singapore
[25] Singapore Immunology Network, Agency for Science, Technology, and Research, Singapore, Republic of Singapore
[26] Department of Microbiology and Immunology, Immunology Translational Research Programme, Yong Loo Lin School of Medicine, National University of Singapore, Singapore, Republic of Singapore
[27] School of Biological Sciences, Nanyang Technological University, Singapore, Republic of Singapore
[28] Genetics of B cells and Lymphoma unit, IFOM ETS-The AIRC institute of Molecular Oncology, Milano, Italy
[29] Department of Molecular Medicine, University of Padova, Padova, Italy
[30] Pathology Unit, IRCCS San Raffaele Scientific Institute, Milan, Italy
[31] Department of Medicine, Weill Cornell, New York, NY, USA
[32] Bruker Spatial Biology, Seattle, WA, USA
[33] Department of Medical Biotechnology and Translational Medicine, University of Milan, Italy
[34] Department of Haematology-Oncology, National University Health System, Singapore, Singapore
[35] NUS Centre for Cancer Research, Yong Loo Lin School of Medicine, National University of Singapore, Singapore, Singapore
[36] Department of Medicine, Yong Loo Lin School of Medicine, National University of Singapore, Singapore, Singapore
[37] Department of Oncology and Hemato-Oncology, University of Milan, Italy

[§] equally contributing authors

Address correspondence to:
Claudio Tripodo, Advanced Pathology Laboratory, IFOM ETS-The AIRC Institute of Molecular Oncology, Via Adamello 16, 20139 Milan, Italy. Phone: +39 02 57430 3816;
Email: claudio.tripodo@ifom.eu. Or to: Anand D. Jeyasekharan, Cancer Science Institute of Singapore, Centre for Translational Medicine 14 Medical Drive, #12-01 Singapore 117599. Phone: +6565167281; Email: csiadj@nus.edu.sg. Or to: Stefano Casola, Genetics of B Cells and Lymphoma Unit, IFOM ETS-The AIRC Institute of Molecular Oncology, Via Adamello 16, 20139 Milan, Italy. Phone: +39 02 57430 3714; Email: stefano.casola@ifom.eu

ABSTRACT (210/210)

The germinal center (GC) dark zone (DZ) and light zone (LZ) represent distinct anatomical regions in lymphoid tissue where B-cell proliferation, immunoglobulin diversification, and selection are coordinated. Diffuse Large B-cell Lymphomas (DLBCL) with DZ-like gene expression profiles exhibit poor outcomes, though reasons are unclear and are not directly related to proliferation. Physiological DZs exhibit an exclusion of T-cells, prompting exploration for whether T-cell paucity contributes to DZ-like DLBCL. We used spatial transcriptomic approaches to achieve higher resolution of T-cell spatial heterogeneity in the GC and to derive potential pathways that underlie T-cell exclusion. We showed that T-cell exclusion from the DZ was linked to DNA damage response (DDR) and chromatin compaction molecular features characterizing the spatial DZ signature, and that these programs were independent of AID deaminase activity. As ATR is a key regulator of DDR, we tested its role in the T-cell inhibitory DZ transcriptional imprint. ATR inhibition reversed not only the DZ transcriptional signature but also DZ T-cell exclusion in DZ-like DLBCL *in vitro* microfluidic models and in *in vivo* samples of murine lymphoid tissue. These findings highlight that ATR activity underpins a physiological scenario of immune silencing. ATR inhibition may reverse the immune silent state and enhance T-cell based immunotherapy in aggressive lymphomas with GC DZ-like characteristics.

INTRODUCTION

Tumors employ diverse strategies to evade the immune system, ranging from altering their intrinsic properties to manipulating their microenvironment (1). Evasion mechanisms include tumor cell expression of inhibitory immune checkpoint molecules (2), recruitment of immunosuppressive cell subsets (3, 4), and modification of the extracellular matrix to impede immune cell function (5, 6). T cells contribute to anti-tumor immunity and are also central to multiple immunotherapy approaches, including checkpoint blockade and adoptive cell therapies (1). Understanding the mechanisms that govern T-cell exclusion within the tumor microenvironment is essential for improving treatment response and immunotherapeutic efficacy.

In epithelial cancers, T-cell exclusion has been linked to stromal remodeling and activation of cell-intrinsic pathways such as WNT/β-catenin, TGF-β, and PI3K signaling (7–11). In contrast, the mechanisms underlying T-cell exclusion in hematologic malignancies like diffuse large B-cell lymphoma (DLBCL) remain poorly defined. Unlike epithelial tumors, lymphomas lack structured tumor-stroma boundaries, posing challenges in delineating spatial immune barriers. While several immune escape mechanisms in lymphoma have been identified, including loss of MHC molecules and constitutive PD-L1 expression (12, 13), the complete range of strategies these lymphomas use to evade T-cell-mediated immunity is still unclear. Poor prognostic DHITsig+ lymphomas display fewer T cells (14, 15), but mechanisms are also not fully defined. Similarly, DZ-like lymphomas resemble the dark zone of the germinal center, thus we turned to germinal centers (GCs) in lymphoid organs as a model system to explore the basis of T-cell exclusion in an homogeneous cellular context (16–18). Although not physically separated, the GC is functionally organized into two distinct regions: the dark zone (DZ), where B cells proliferate and mutate their antibody variable genes, and the light zone (LZ), where B cells engage other immune cells, including T follicular helper cells, to refine antibody affinity (19, 20). This natural segregation of cellular activities within the GC provides an ideal setting to study factors influencing T cell distribution.

Using quantitative immunohistochemistry (IHC), digital spatial profiling, and single-cell spatial transcriptomics, we examined the *in situ* microenvironment of the GC LZ and DZ area, detailing their relationship with T-cell localization and phenotype. We identified the LZ/DZ interface as a barrierless constraint limiting homogeneous intra-GC T-cell distribution. T-cell exclusion was recapitulated in Diffuse Large B-cell Lymphomas (DLBCLs) expressing a GC DZ gene signature, suggesting a link between GC biology and tumor immune evasion. Spatial transcriptomics analysis revealed preferential activation of DNA damage response (DDR) pathways and suppression of inflammatory signaling in the DZ, correlating with increased chromatin compaction. We identify the Ataxia Telangiectasia and Rad3 related (ATR) kinase as a central regulator of these pathways, sustaining the DZ transcriptional program and promoting T-cell exclusion. These findings position ATR as a central player in spatial regulation of the GC reaction and point to potential mechanisms that may be co-opted by a subset of DLBCLs to facilitate immune evasion.

RESULTS

Spatial profiling reveals distinct transcriptional programs in germinal center DZ and LZ regions

Reactive GCs display spatial compartmentalization, with a proliferative, Ki-67-dense DZ and a follicular dendritic cell (FDC)-rich LZ, bordered by T-cell-dense extrafollicular regions (Figure 1A). Spatial analysis highlighted significant exclusion of $CD3^+$ T cells from the AID-marked DZ, evidenced by an increased CD3-to-AID distance compared to a random spatial distribution (Figure 1B-C, Supplementary Figure 1A). In contrast, $CD68^+$ macrophages were uniformly distributed across both zones (Figure 1D, Supplementary Figure 1B-C), serving as a control that supports the specificity of T-cell exclusion from the DZ.

To investigate the molecular programs underlying T-cell exclusion from the DZ, we performed spatial transcriptional profiling of reactive GCs. DZ and LZ regions were defined using the B-cell marker CD20 and the LZ marker CD271/NGFR (Figure 1E). Digital Spatial Profiling (DSP) was chosen for its ability to capture spatially resolved gene expression while preserving tissue architecture. Using the GeoMx Cancer Transcriptome Atlas, we analyzed 1,824 immune- and tumor-related genes in matched GC DZ and LZ regions from human tonsils (n = 10 pairs) (21).

This analysis identified a robust DZ/LZ transcriptional signature composed of 370 differentially expressed genes (adjusted $p < 0.05$), with 169 upregulated in the DZ and 201 in the LZ (Figure 1F-G, Supplementary Table 1). Pathway enrichment revealed functionally distinct profiles: DZ regions were enriched for DDR, cell cycle progression, and DNA replication stress, while LZ regions were enriched for immune signaling pathways (Figure 1H-I, Supplementary Table 2). Given their spatial origin, our DZ and LZ signatures encompass transcripts from multiple cell types. To validate that these signatures adequately represent the biology of DZ and LZ B cells, we applied them to a whole-transcriptome single-cell RNA-sequencing dataset of germinal center B cells (GSE139891) (Supplementary Figure 1D) (17). The signatures effectively distinguished DZ from LZ B-cell populations, confirming that they also capture B-cell transcriptional states. While this provides orthogonal validation, the primary strength of our approach lies in its spatial resolution, enabling analysis across the full tissue context—including non–B-cell contributions.

As an additional validation, we performed an independent whole-transcriptome (WTA) DSP and compared DZ and LZ regions. We used two gene lists to classify germinal center B cells

into DZ and LZ types: the spatial DZ/LZ signature and the differentially expressed genes (DEGs) identified through the WTA DSP. The spatial DZ/LZ signature showed greater predictive power than the WTA DEGs, confirming its strong discriminatory capacity (Supplementary Figure 1E).

Spatial heterogeneity of T-cell distribution within the germinal center

To investigate the spatial organization of T-cell subsets in lymphoid tissue, we applied a single-cell–resolved spatial whole-transcriptome (WTX) approach using the CosMx Spatial Molecular Imager (SMI) platform across nine human tonsillar GCs. Previous iterations of CosMx SMI enabled profiling of up to 6,000 RNA targets; the latest version allows detection of over 18,000 transcripts, enabling comprehensive spatial transcriptomics at both single-cell and subcellular resolution. Cell type annotation was performed via label transfer from a well-annotated single-cell RNA sequencing (scRNA-seq) reference dataset (HCATonsilData) using MaxFuse, a cross-modality integration algorithm. This strategy enabled robust identification of transcriptionally defined immune populations—including T-regulatory (Treg), T-follicular helper (Tfh), memory, $CD8^+$ effector, naïve $CD8^+$, and CD4/CD8 double-negative (DN) T cells—within the architectural context of the GC (Figure 2A) (22).

DZ and LZ regions were independently segmented based on spatial transcriptomic signatures. We first confirmed that the DSP-derived DZ and LZ signatures could accurately define corresponding regions within the CosMx datasets, providing orthogonal spatial validation across platforms (Figure 2B, Supplementary Figure 2A). With these defined compartments, we next investigated the distribution of T-cell subsets within each region, enabling precise mapping of immune cell populations relative to the DZ–LZ boundary (Figure 2C). Most active T-cell subsets—Tregs, Tfh, $CD8^+$ T cells, and memory T cells, were enriched in the LZ. In contrast, naïve $CD8^+$ and DN T cells showed no compartmental preference (Figure 2D). Naïve $CD8^+$ T cells were defined by high expression of CD8 and CCR7, and low expression of activation and memory-associated genes, including HLA-DRB1, GZMA, LAG3, IFNG, and CD99; all non-naïve $CD8^+$ cells were classified as $CD8^+$ T cells.

The spatial trends were corroborated at the protein level using hyperplexed immunofluorescence with the MACSima platform, which demonstrated significant LZ enrichment for Tfh and memory T-cell subsets ($CD4^+$ and $CD8^+$), while DN and naïve $CD4^+$/$CD8^+$ T cells showed no significant association with either compartment (Figure 2E, Supplementary Figure 2B-C). The lack of LZ enrichment for naïve $CD8^+$ and DN T cells—populations not expected to be actively engaged in MHC-dependent interactions—was consistent with the reduced expression of MHC molecules in DZ B cells compared to those in the LZ (Figure 2F-G, Supplementary Table 3).

Since DN T cells include a substantial fraction of γδ T cells, we further examined their localization within GCs. Immunohistochemistry for γδTCR revealed rare γδ T cells, which were preferentially enriched in the DZ (Supplementary Figure 2D-E) (23).

To further assess the spatial positioning of T cells relative to B-cell subtypes, we quantified the proximity of $CD4^+$ and $CD8^+$ T cells to $PLK1^+$ DZ B cells and $EGR1^+$ LZ B cells—representative markers derived from our spatial transcriptional signatures. (Supplementary Figure 2F-I). Both T-cell types were located closer to LZ B cells, consistent with their LZ enrichment. However, $CD8^+$ T cells exhibited markedly shorter distances to DZ B cells than $CD4^+$ T cells. This proximity correlated with increased expression of IFNγ among $CD8^+$ T cells,

with IFNγ$^+$ cells preferentially localized at the DZ–LZ interface (Supplementary Figure 2J-L), suggesting that effector CD8$^+$ T cells accumulate at GC boundaries where they may be poised for functional engagement.

Together, these findings reveal compartment-specific localization of T-cell subsets, with functional CD8$^+$ T cells concentrating at the GC interface and naïve or DN T cells distributing independently of GC zonation.

The GC DZ spatial signature negatively correlates with T cell gene programs and clinical outcome in DLBCL

DZ-associated gene signatures, including the double-hit signature (DHITsig), and the molecular high-grade (MHG) signature, are linked to high-grade B-cell lymphomas with poor prognosis and reduced T cell abundance (14, 15). DHITsig was originally identified in high-grade B-cell lymphoma with MYC and BCL2 rearrangements (HGBCL-DH-BCL2). We have previously shown that a spatial GC DZ signature clusters aggressive lymphoma types (MHG and DHIT) and correlates with poor prognosis (18). To investigate whether lymphomas exhibiting high DZ spatial signature expression display similar T-cell depletion patterns, we analyzed transcriptomic data from 3,610 DLBCL cases across eight independent cohorts (GSE32918; GSE98588; GSE87371; GSE10846; Reddy; Schmitz; GSE117556; GSE31312) (24–31). Using xCell transcriptional deconvolution (32), we found that DZ-like cases had reduced frequencies of most T-cell populations, except for CD8$^+$ and γδ T cells, recapitulating the patterns observed in reactive GCs (Figure 3A).

Next, we assessed the prognostic significance of the DZ and LZ spatial signatures by analyzing transcriptomic data from 1,078 aggressive B-cell lymphomas, harmonized from two well-annotated RNA-seq datasets (GSE117556; GSE32918). Based on the expression of the DZ/LZ spatial signature, we classified the samples into DZ-like, LZ-like, and intermediate groups. UMAP projection of these groups confirmed distinct expression patterns (Figure 3B). DZ-like cases were associated with significantly shorter overall survival (OS) (Figure 3C, Supplementary Figure 3A), a trend that remained consistent across germinal center B-cell (GCB) and activated B-cell (ABC) subtypes (Supplementary Figure 3B-E). Analysis of 35 DHL cases revealed that those with a high DZ signature exhibited the lowest expression of the T-cell signature, further supporting that the GC DZ signature captures a DZ-like biology in aggressive B-cell lymphomas involving attenuated T-cell infiltration (Supplementary Figure 3F).

To determine whether the inverse correlation between DZ spatial signature expression and T-cell infiltration holds true at the level of intra-tumoral heterogeneity, we performed DSP on 11 regions of interest (ROIs) from a single DLBCL lymph node biopsy (Figure 3D, Supplementary Table 4). Immune cell composition analysis revealed a strong inverse correlation between DZ signature expression and T-cell abundance (Figure 3E-F), with no significant associations detected for other immune cell populations (Supplementary Figure 3G). Visualization of CD3 staining showed reduced T-cell density in regions with high DZ signature expression, supporting the inverse correlation (Figure 3G).

To assess whether this spatial relationship holds across a larger cohort, we analyzed an independent cohort of 103 DLBCL tissue microarray (TMA) samples profiled by DSP whole-transcriptome analysis using B-cell (CD20$^+$) and T-cell (CD3$^+$) morphological windows (Figure 3H) (33). Consistent with the intra-tumoral profiling data, higher DZ signature expression

correlated with lower abundance of CD3 areas of interest (AOI) nuclei counts (Figure 3I). This association was further confirmed by multiplex immunohistochemistry in 79 of the DLBCL cases, which confirmed that $CD20^+$ tumor regions with elevated DZ signature expression displayed reduced $CD3^+$ T-cell density (Figure 3J).

These results establish a direct association between the DZ spatial transcriptional program and T-cell exclusion in both reactive GCs and DLBCL.

The GC DZ spatial signature is independent of AID-induced mutagenesis

AID plays a crucial role in DNA mutagenesis during immunoglobulin (IG) somatic hypermutation and contributes to the epigenetic heterogeneity of GC B cells (34). To determine whether AID activity is required to maintain the spatial DZ transcriptional signature, we analyzed GCs from Aicda-deficient (*Aicda*$^{tm1(cre)Mnz/J}$) mice, where the endogenous Aicda coding sequence is replaced with a Cre recombinase cassette (35). Cre expression was uniform across GC B cells in *Aicda*$^{-/-}$ mice, confirming effective knockout and providing a surrogate marker for Aicda locus inactivation (Figure 4A-B). Spontaneous GCs in the mesenteric lymph nodes (mLNs) of *Aicda*$^{-/-}$ mice were larger and had an increased fraction of Ki-67^+ proliferating cells compared to wild-type (WT) controls, consistent with prior findings that loss of AID results in impaired clonal selection and accumulation of proliferative centroblasts (Figure 4A,C) (36).

To further investigate the impact of AID deficiency on the DZ signature, we conducted spatial transcriptomic profiling using Visium methodology on 1,950 microregions from mLNs of WT (n = 1,270) and *Aicda*$^{-/-}$ (n = 680) mice (Figure 4D). Unsupervised clustering identified seven transcriptionally distinct regions in WT mLNs and five in *Aicda*$^{-/-}$ mLNs (Supplementary Figure 4A-D, Supplementary Table 5). Differential expression analysis of follicle/GC clusters revealed 1,007 differentially expressed genes (392 upregulated in WT and 615 in *Aicda*$^{-/-}$ GCs) (Figure 4E-F, Supplementary Table 6). As expected, *Igha* expression was elevated in WT GCs, whereas *Ighm* was upregulated in *Aicda*$^{-/-}$ GCs, consistent with the loss of IG class-switch recombination in mutant cases.

Importantly, the *Aicda*$^{-/-}$ follicular/GC microregions were globally enriched for the DZ spatial signature compared to WT counterparts (Figure 4G, Supplementary Figure 4E, Supplementary Table 7). This enrichment was accompanied by lower T-cell signature expression (Figure 4H), which was further confirmed by immunohistochemical staining of CD4 and CD8 in total GCs and DZ/LZ regions (Figure 4I-L, Supplementary Figure 4F-G). These results suggest that the DZ transcriptional program is independent of AID activity and that AID deficiency does not prevent T-cell exclusion.

To investigate the transcriptional characteristics of the DZ signature independent of AID activity, we analyzed scRNA-seq data from human GC DZ B cells (GSE139891), stratified into AICDA-high (AICDA expression > tertile 2) and AICDA-low (undetectable AICDA expression) groups (Supplementary Figure 4H). AICDA-high DZ cells exhibited significantly higher expression and enrichment of the DZ spatial signature compared to AICDA-low DZ cells (Figure 4M, Supplementary Table 7). Pathway analysis revealed that AICDA-high DZ B cells were enriched for genes involved in the G2/M cell cycle phase (Figure 4N, Supplementary Figure 4I, Supplementary Table 8), whereas AICDA-low DZ B cells showed enrichment in DNA replication machinery genes, and ATR-mediated replication stress pathways (Figure 4O, Supplementary Table 8).

These results suggest that ATR-mediated replication stress may contribute to the DZ transcriptional program and its associated T-cell exclusion, independent of AICDA-induced mutagenesis.

ATR inhibition rewires DZ programs enabling a T-cell permissive environment

Given the potential importance of ATR in maintaining DZ identity in an AID independent manner, we further evaluated ATR-dependent pathways within the GC. DZ transcriptional profiling revealed an ATR-dependent activation of DDR and repair pathways. ATR is a key regulator of the cellular response to replication stress, playing a pivotal role in preserving chromatin organization and in restraining activation of the cGAS-STING pathway (37–39). ATR likely controls these key components of the DZ spatial signature (Supplementary Figure 5A-B, Supplementary Table 9).

Consistent with this, DZ B cells exhibited enrichment for chromatin remodeling and nuclear stability markers, including RAD51, γH2AX (phospho-S139-H2AX), phospho-S824-KAP1, SMARCA4 (BRG1), EZH2, and heterochromatin-associated markers H3K9me3 and HP1 (Supplementary Figure 5C). Furthermore, DZ B cells displayed features of chromatin compaction, as indicated by higher minimum DAPI intensity extracted from nuclear morphology and chromatin organization (NMCO) features in DAPI-labeled GCs (Supplementary Figure 5D-E) (40). Heterochromatin features were predictive of DZ identity, as a random forest model trained on NMCO features accurately classified DZ and LZ B cells (Supplementary Figure 5F), and correlated positively with DZ signature expression in DLBCLs (Supplementary Figure 5G).

Nuclear stability restricts cGAS-STING pathway activation, and we found that DNA and RNA sensing pathways were predominantly LZ-restricted (Supplementary Figure 5H, Supplementary Table 9). Proximity ligation assay (PLA) confirmed cGAS localization to the LZ, with minimal activity in the DZ (Supplementary Figure 5I-J), supporting the notion that the DZ is an immune "cold" environment, relatively resistant to inflammatory stimuli.

To investigate the role of ATR in maintaining the DZ transcriptional program, we treated two DZ-like lymphoma cell lines, HT and SUDHL-5 (Supplementary Figure 6A), with the ATR inhibitor (ATRi) Ceralasertib (AZD6738) or DMSO control for 48 hours (Figure 5A, Supplementary Table 10). At 1μM concentration, ATR inhibition did not impact cell viability (Supplementary Figure 6B-C). ATRi treatment significantly increased micronuclei formation, a precursor to cGAS-STING activation (Figure 5B-C) (41). Moreover, ATRi-induced transcriptional changes (Supplementary Table 11) included upregulation of interferon-stimulated genes and MHC-I/II transcripts, reversing the immune-evasive profile of DZ-like DLBCLs (Figure 5D, Supplementary Table 7). Notably, ATRi-treated DLBCL cells revealed a shift in transcriptional identity, with enrichment of the LZ spatial signature and suppression of the DZ spatial signature, suggesting that ATR activity reinforces the DZ transcriptional program (Figure 5E, Supplementary Table 7).

Next, to explore the potential impact of ATR inhibition on immune cell recruitment, we performed a competitive microfluidic assay (42, 43), co-culturing peripheral blood mononuclear cells (PBMCs) from healthy donors with ATRi- or DMSO-treated HT and SUDHL-5 DZ-like DLBCL cells (Figure 5F). After 24 and 48 hours, PKH26-labeled PBMCs showed significantly increased infiltration into ATRi-treated chambers (Figure 5G-J). Fluorescence

microscopy revealed direct interactions between infiltrating $CD3^+$ T cells and ATRi-treated DLBCL cells (Figure 5K-L).

To evaluate the effect of enhanced T cell recruitment through ATR inhibition in a model representing the patient DLBCL immune context, we utilized primary cell lines derived from patient-derived tumor xenografts (PDXs). Among 22 PDX tumor samples, two were selected based on their DZ-LZ spatial signature expression: one DZ-like sample (high DZ, low LZ expression) and one LZ-like sample (low DZ, high LZ expression) (Figure 5M, Supplementary Methods). T-cells were expanded by co-culturing PBMCs with corresponding irradiated (10 Gy) PDX cell lines, and the expanded T-cells were subsequently harvested. T-cell killing assays were performed across a range of effector-to-target (E:T) ratios, in which LZ-like DLBCL cells displayed greater sensitivity to T cell-mediated killing compared to the DZ-like DLBCL cells. Importantly, ATRi pretreatment (1 μM and 5 μM) remarkably enhanced T-cell killing of DZ-like DLBCL cells (Figure 5N), whereas LZ-like DLBCL cells (Figure 5O), which were already sensitive, showed no further improvement.

These results show that ATR inhibition reprograms DZ-like DLBCLs and attenuates their immune-silent state, facilitating increased T-cell interaction and susceptibility to cytotoxicity.

ATR Inhibition promotes T-cell infiltration in the GC microenvironment

To validate these findings *in vivo*, we treated a total of 14 BALB/c mice with 25 mg/kg ATRi ($n = 4$ per timepoint) or vehicle control ($n = 2$ per timepoint) for either 2 or 5 consecutive days, and harvested mLNs the following day. After 5 days of treatment, ATRi-treated mice exhibited a significant increase in $CD3^+$ T-cell infiltration within chronic, spontaneously formed mLN GCs compared to vehicle-treated controls (Supplementary Figure 7A).

In a complementary experiment, C57BL/6 mice were immunized with the T-cell-dependent antigen NP-OVA to induce GC formation (Figure 6A). Two days post-immunization, mice ($n = 5$ per group) were treated with either 50 mg/kg ATRi or vehicle control for 5 consecutive days, and lymphoid tissues were harvested the following day. Immunohistochemical staining of mLN sections for Ki-67 and CD3 revealed a higher number of $CD3^+$ T cells per GC in ATRi-treated mice relative to controls (Figure 6B-C; Supplementary Figure 7B, D).

Triple staining for CD3, CD21 and Ki-67 enabled spatial mapping of T cells within GC compartments, distinguishing the DZ ($Ki\text{-}67^+CD21^-$) from the LZ ($CD21^+$). This analysis revealed that T-cell infiltration occurred predominantly in the DZ, with no significant increase in the LZ (Figure 6D). Additional staining for CD4 and CD8 was performed to define the subset of infiltrating T cells, revealing increased numbers of both T-cell subsets within GCs across both mouse models, with DZ-infiltrating T cells primarily composed of activated *Ifnγ*$^+$ $CD8^+$ cytotoxic T cells (Figure 6B,E,F,G; Supplementary Figure 7C,E,F).

Consistent with increased cytotoxic T-cell infiltration, mRNA *in situ* hybridization (*ISH*) revealed induced *Ifnb1* expression in DZ B cells of ATRi-treated mice (Figure 6F,H; Supplementary Figure 7C,G), indicating activation of a localized type I interferon response within the DZ microenvironment. Given the role of type I interferons in promoting antigen presentation, we assessed MHC class I protein expression by quantitative IHC. ATRi-treated mice exhibited a significant MHC-I enrichment in GC DZ regions, supporting a role for ATR in

maintaining immune silencing by restricting $CD8^+$ T-cell recognition (Figure 6F,I; Supplementary Figure 7C,H).

Together, these *in-vivo* results indicate that ATR inhibition perturbs the immune-silent status of the GC DZ, inducing local type-I interferon, enhanced MHC expression and cytotoxic T-cell recruitment.

DISCUSSION

In this study, we used high-resolution spatial transcriptomics to interrogate the immune architecture of the germinal center, with a particular focus on T-cell positioning. Using single-cell–resolved WTX via the CosMx platform, we uncovered substantial spatial heterogeneity in T-cell distribution across the GC. Most T-cell subsets—including Tfh, Treg, and memory $CD8^+$ T cells—were preferentially enriched in the LZ, while CD4/CD8 DN and naïve $CD8^+$ T cells showed no zone-specific enrichment. These findings were confirmed at the protein level using hyperplexed immunofluorescence (MACSima), reinforcing the idea that the LZ serves as the primary site of T-cell–B-cell interaction within the GC, whereas the DZ remains largely T-cell excluded.

To understand the molecular basis of this compartmental organization, we leveraged Digital Spatial Profiling to derive a spatially-accurate signature for the DZ and LZ regions based on transcriptional profiling. Our analysis revealed distinct transcriptional programs in these zones, with the DZ marked by upregulation of DNA damage response, cell cycle, and DNA replication stress pathways, while the LZ was enriched in immune signaling networks. These spatial gene expression programs, coupled with the exclusion of T cells from the DZ, suggested a functional compartmentalization that may be retained in GC-derived lymphomas.

DHIT and MHG B-cell lymphomas—which exhibit DZ-like transcriptional features—tend to have reduced T-cell infiltration (14, 44); however, the contribution of spatially defined DZ signatures to this immune-cold phenotype had not been directly examined. Using our GC-derived DZ signature, we stratified DLBCL cases and found that tumors with high DZ signature expression were consistently associated with low T-cell abundance. These results suggest that DZ-like lymphomas may be intrinsically resistant to T cell–mediated immunotherapies, such as bispecific antibodies and CAR T cells, due to an underlying biology of immune exclusion rooted in their spatial programming (45).

A key mechanistic insight from our work involves the DNA damage response kinase ATR. ATR is known to orchestrate the replication stress response in the GC DZ, preserving nuclear integrity during rapid proliferation (39). It has also been implicated in modulating immune responses in other cancers, where ATR inhibition can promote T-cell recruitment and enhance immune activation (46, 47). However, its specific role in shaping the immune landscape of the GC—and of DZ-like lymphomas—has not been previously defined. *In vivo*, ATR inhibition disrupted the immune-silent character of the GC DZ, reinforcing its role as a key regulator of T-cell exclusion. Treatment with ATR inhibitors led to selective infiltration of $CD4^+$ and $CD8^+$ T cells into the DZ, accompanied by activation of cytotoxic $CD8^+$ T cells and induction of type I interferon signaling. Notably, this was associated with increased MHC-I expression on DZ B cells, suggesting that ATR normally functions to suppress antigen presentation and limit local immune activation (48). These findings support a model in which ATR activity reinforces the proliferative, immune-protected state of the DZ by actively suppressing cues that would otherwise recruit and engage T cells. By lifting this suppression,

ATR inhibition reprograms the DZ into an immune-permissive environment, enhancing T-cell access and effector function. This mechanism may extend to DZ-like DLBCLs, which similarly exhibit low T-cell infiltration, and highlights ATR inhibition as a rational strategy to sensitize these tumors to T cell–based immunotherapies.

MATERIALS AND METHODS

Sex as a biological variable

Our study examines both male and female human reactive tonsil samples and animals in a balanced manner. Animals of both sexes were randomly assigned to experimental groups to ensure unbiased representation. Throughout the course of the study, no significant sex-dependent differences were observed in any of the measured parameters.

Collection and handling of human tissue samples

Formalin-fixed and paraffin-embedded (FFPE) samples of human tonsils with reactive follicular hyperplasia (*n* = 20) were selected from the archives of the Tumor Immunology Unit, University of Palermo, for *in situ* quantitative IHC and IF, mRNA ISH and PLA analyses. One FFPE lymph node tissue sample involved by DLBCL was collected from the archives of the Pathology Unit of the University of Brescia for quantitative IF analyses and digital spatial profiling of microregions from DLBCL-infiltrated areas.

Murine models

Aicda$^{tm1(cre)Mnz/J}$ (JAX:007770) and Wild Type C57BL6/J mice were obtained from Jackson Laboratory. Animals were regularly monitored by veterinary personnel throughout the duration of the experiments. Mice were checked at least three times a week for signs of illness and any reduction or impairment in motility. The experimental mice were followed until they reached 28-32 weeks of age. At this point they were euthanized to collect mesenteric lymph nodes for histopathological, immunolocalization and spatial transcriptomic analyses.

Male Balb/c mice (InVivos Singapore) were randomly assigned to vehicle control (*n* = 2) or ATRi treatment (*n* = 4) groups. AZD6738, an ATR inhibitor, was dissolved at 2.5 mg/mL in a vehicle solution containing 10% DMSO, 40% propylene glycol, and 50% deionized sterile water. Mice in the treatment group received 25 mg/kg AZD6738 by oral gavage daily for either 2 or 5 consecutive days. Tissues were harvested on day 3 or day 6, respectively. Control mice received an equivalent volume of vehicle solution.

In a separate experiment, 6-week old male C57BL/6J mice (Jackson Laboratory) were immunized intraperitoneally with 4-Hydroxy-3-nitrophenylacetyl-conjugated ovalbumin (NP-OVA) adsorbed on alum. Two days post-immunization, mice (*n* = 5 per group) received daily 50 mg/kg AZD6738 by oral gavage for 5 consecutive days. Spleens and mesenteric lymph nodes were harvested 24 hours after the final dose. All harvested tissues were immediately fixed in cold 10% neutral buffered formalin (NBF) for 12 hours, followed by standard paraffin embedding procedures.

PDX-derived primary cell lines and in vitro killing assay

22 primary DLBCL tumor samples were implanted subcutaneously into NSG-S mice (Jackson Laboratory) to generate PDX models (49). Once tumors reached the appropriate size, they were excised, enzymatically and mechanically digested, and cultured in RPMI-1640 medium supplemented with 10% fetal bovine serum (FBS) and IL-2. After stabilization *in vitro*, samples were ranked based on the expression of the DZ and LZ signature, from which 1 DZ-like and 1 LZ-like sample was used for downstream experiments. T cells were expanded by co-culturing peripheral blood mononuclear cells (PBMCs) with 10 Gy irradiated DLBCL tumor cells in RPMI-1640 supplemented with 10% FBS, IL-2, IL-7, and IL-15. Expanded T cells were harvested and used in cytotoxicity assays. PDX-derived DLBCL cells were treated with the ATR inhibitor Ceralasertib at two concentrations (1 μM and 5 μM) or DMSO for 4 days. Following treatment, 1×10^5 tumor cells were plated per well in 96-well plates. Expanded T cells were added at varying effector-to-target (E:T) ratios. After 72 hours of co-culture, cells were stained with anti-CD3, anti-CD19, and DAPI, and analyzed by flow cytometry to quantify T cell-mediated tumor killing.

DLBCL cell culture and treatment

HT and SUDHL-5 cell lines were obtained from the ATCC and selected based on the high expression of the DZ spatial signature according to the 23Q2 DepMap gene expression dataset. HT and SUDHL-5 cells were cultured in RPMI media supplemented with 1% glutamine, 10% fetal bovine serum (FBS) and penicillin-streptomycin. Suspension cultures were maintained in flasks in 5% CO_2, at 37°C. The cells were treated for 48 hours with clinical-grade ATR inhibitor Ceralasertib (AZD6738, S7693 Selleckchem, 1 μM) and DMSO for the untreated control. Cell lines were obtained from ATCC and tested for mycoplasma contamination, with negative results. Additional information on micronuclei analysis, RNA extraction, qPCR, and RNAseq is available in the Supplementary Methods.

Competitive migration assay in microfluidic devices

Microfluidic devices were fabricated in PDMS (polydilmethylloxane), a bio compatible silicon elastomer, as previously reported (50). The device allowed visualization of preferential PBMC migration towards ATRi- or DMSO-treated HT and SUDHL-5 cells embedded in 3D hydrogels. Additional information on cell loading, labeling, and quantitative analysis is available in the Supplementary Methods.

Hyperplexed MACSima analysis

Multiplex immunofluorescence analyses were performed on FFPE tonsil sections using the MACSima platform (Miltenyi Biotec) (51). Tissue sections were processed and stained in a fully automated manner, with sequential immunolabeling, imaging, and quantification analyses. Further details on the protocol and antibody panel are provided in the Supplementary Materials.

Quantitative in situ hybridization and immunolocalization analyses

Single and multiplexed IHC and IF stainings, and *in situ* mRNA ISH were performed on FFPE human or murine tissue sections as previously described (52). The detailed protocol and antibodies adopted are included in the Supplementary Methods. IHC-stained slides were digitalized using an Aperio CS2 digital slide scanner (Leica Microsystems) and IF-stained slides were analyzed and imaged under a Zeiss Axioscope-A1 equipped with widefield fluorescence module and Axiocam 503 Color camera (Zeiss). Quantitative analyses was performed using HALO image analysis software for cell segmentation and signal quantification (v3.2.1851.229, Indica Labs) as detailed *Spatial Analysis* paragraph of the Supplementary Methods.

In situ Proximity Ligation assay (PLA)

PLA was conducted on FFPE sections from human tonsil samples using the NaveniFlex Tissue MR Red kit following manufacturer's instructions (Navinci Diagnostics). The list of antibodies adopted for test and control PLA assays is included in the Supplementary Methods. Quantitative analysis of PLA signals was performed through HALO image analysis software (v3.2.1851.229, Indica Labs) as detailed in the Supplementary Methods.

In situ transcriptional analyses

10 DZ and LZ regions of interest (ROIs) within morphologically normal formalin-fixed paraffin-embedded (FFPE) human tonsillar GCs were profiled using the GeoMx® Digital Spatial Profiler (NanoString Technologies, Seattle, Washington, USA). Tissue sections were stained with CD271/NGFR and CD20, as described in our previous work (21). The selected and segmented DZ and LZ ROIs were analyzed for the expression of 1,824 curated genes included in the Cancer Transcriptome Atlas (CTA) panel.

Spatial transcriptomics of DLBCL tissues was performed using the GeoMx Whole Transcriptome Atlas (WTA) kit (NanoString, Seattle, Washington, USA), according to the manufacturer's protocol. FFPE tissue sections were processed on the Leica Bond Max automated system, followed by *in situ* hybridization. Sections were stained with CD3 and CD20 to visualize T and B cells, respectively. ROIs were selected based on pathologist recommendations and analyzed using the GeoMx DSP platform. $CD3^+$ and $CD20^+$ signal masks were generated and submitted for downstream sequencing and data processing. Full details of the DSP workflow, including ROI selection, library preparation, sequencing, and data normalization, are provided in our previous work (33).

Additionally, 11 ROIs were selected from a DLBCL-infiltrated FFPE lymph node tissue sample based on CD20 and CD3 staining and profiled using the same CTA panel. Further information on DSP data analysis is provided in the Statistical and Bioinformatics Analyses section and in the Supplementary Methods.

For murine tissue analysis, spatial transcriptomics was performed on FFPE mesenteric lymph nodes using the 10x Genomics Visium platform, following the manufacturer's instructions. Details regarding library preparation, sequencing, and data analysis for the Visium experiment are available in the Supplementary Methods.

CosMx Whole Transcriptome Atlas

Processing of Data

CosMx SMI Whole Transcriptome WTX was shared with us from Bruker Spatial Biology as a Seurat object. The QC filters were applied, retaining cells with than nFeature_RNA counts < 3000 and nCount_RNA > 400. Filtered dataset was then converted to the AnnData format for downstream analysis with Python-based Scanpy. Final dataset has 132,676 cells across 18,935 targets.

Data Normalization

The top 5000 highly variable genes were identified with scanpy.experimental.pp.highly_variable_genes function which uses Pearson residuals as basis for selection. The data was then log transformed and scaled. Scaled values were subjected to principal component analysis (PCA) for linear dimension reduction. A nearest neighbor network was created based on Euclidean distances between cells in a multidimensional PC space (the first 50 PCs were used). For visualization, the Uniform Manifold Approximation and Projection (UMAP) technique was employed.

Annotation of germinal centers

Germinal centers (GC) were identified based on expression of 7 GC B cell markers (BCL6, AICDA, CD38, LMO2, MEF2B, PIM1, ST6GAL1 and EZH2) and DAPI intensities derived from immunofluorescence images in the CosMx experiment. The expression levels of GC B cell markers and DAPI intensities were visualized in Napari, where GC regions were manually annotated. Annotation was based on circular clusters exhibiting high GC B cell marker expression and reduced DAPI signal relative to the surrounding cells. In total, nine germinal centers were identified.

DZ and LZ segmentation

The 169-gene DZ signature and 201-gene LZ signature was scored in the dataset and visualized. It was observed that the GCs were polarized based on the DZ and LZ signature. To determine the DZ or LZ status of each individual cell, we subtracted the LZ signature score from the DZ signature score to form a combined DZ-LZ score. A highly positive DZ-LZ score (> 0.3) corresponds to a DZ phenotype (termed DZ cells) and a highly negative DZ-LZ score (< -0.3) corresponds to a LZ phenotype (termed LZ cells). Remaining cells were allocated to an intermediate phenotype.

To identify putative DZ and LZ regions within each GC, an iterative graph-based cell neighbor analysis was performed. Briefly, a spatial graph G was constructed to represent cellular relationships. Each node in G corresponded to a cell, with attributes including x and y coordinates representing its spatial location and a phenotype label derived from previous DZLZ classification. Edges were created between nodes based on Euclidean distance, capturing the local neighbors of each cell. The pairwise Euclidean distances between all cells were precomputed using the SciPy function *cdist*, generating a distance matrix for all cell pairs, allowing for efficient identification of neighboring cells within a fixed spatial threshold.

In each iteration, neighbors of each cell within the GC will be checked and reannotated based on a predetermined fraction of dissimilar neighbors. Cells with an intermediate phenotype were reannotated based on the most common phenotype of their immediate neighbors. The iterative process was repeated until no further changes to cell annotations were made. To maintain an

accurate representation of the DZ and LZ regions, the DZ region was required to contain at least 70% DZ cells, and similarly, the LZ region was required to contain at least 70% LZ cells. Once this condition was met, the boundary between the two regions was established and retained for subsequent downstream spatial analyses.

Label Transfer by MaxFuse

Cell type annotation was achieved by label transfer from a well-annotated reference scRNA-seq HCATonsil dataset. Label transfer was done using MaxFuse, which could integrate data across different modalities such as spatial and suspension single-cell RNA datasets, through cross-modality matching and iterative smoothed embedding. To ensure robust label transfer, the top 5000 highly variable genes common to both the scRNA-seq and CosMx WTX spatial dataset were identified and used as matched pairs. Following label transfer, spatial distributions of subpopulations of T cells were analyzed within the DZ and LZ regions of the germinal centers.

Spatial distribution of T cells

Using the DZ and LZ boundary line as reference, we assessed the distribution of T cell subpopulations from -100μm (DZ) to 100μm (LZ) from the reference line. Cells were binned into 10μm increments based on their distance from the boundary, and the mean enrichment level of each T cell subtype for each bin was computed, providing a continuous spatial profile of T cell subtype enrichment across the boundary. Linear regression coefficient of the observed slope line was used as a measure of spatial distribution pattern across the boundary. To determine whether the observed enrichment trend was significantly different from a random distribution, we performed 10,000 Monte Carlo simulations where cell positions of each subtype were randomly shuffled while ensuring that its total cell count remained fixed. For each iteration, a new linear regression was fitted to the randomized enrichment-distance relationship, generating a null distribution of slopes, under the assumption of Complete Spatial Randomness (CSR). The Monte Carlo confidence envelope was plotted as a shaded region, representing the range of slopes expected under random conditions. A 95% CI was constructed from these simulations:

1. If the observed slope fell above the upper 95% CI, enrichment of the T cell subtype was significantly increasing with distance from DZ into LZ.
2. If the observed slope fell below the lower 95% CI, enrichment of the T cell subtype was significantly decreasing with distance from DZ into LZ.
3. If the observed slope remained within the Monte Carlo envelope, enrichment variation was consistent with randomness.

Computational pipelines to characterize the chromatin states of DZ and LZ cells

Computational analyses were conducted on digital images derived from two datasets: 15 manually identified GCs from AID/CD3 immunofluorescence-stained tissues and 11 DSP-profiled DLBCL ROIs stained for CD20 and CD3. DZ and LZ B cells were classified based on nuclear chrometric features by applying a Random Forest classifier. The relationship between chrometric states and the DZ signature was evaluated in the selected *in situ* transcriptionally-profiled microregions. Additional information on pipeline implementation, image processing, and statistical analyses is available in the Supplementary Methods.

Statistical and bioinformatics analyses

The spatial DZ and LZ signatures were obtained by comparing the gene expression of paired human tonsil DZ and LZ GC ROIs (*n* = 10) profiled by Nanostring Digital Spatial Profiling as previously reported (21). Upregulated/downregulated genes were selected using the limma moderated statistic (53) (BH adjusted p-values < 0.05). The Reactome Pathway library was used for pathway enrichment analysis (ReactomePA R package) (54). The Euclidean distance and the Ward.D2 method were used for unsupervised clustering. The SpatialDecon algorithm (55) was adopted to estimate cell fractions on DSP data, while the xCell algorithm (32) was used to estimate selected immune and stromal cell type enrichment scores on bulk RNA-seq samples. Additional information on unsupervised hierarchical clustering, pathway and gene set enrichment analyses, DZ/LZ Single-cell RNAseq analysis, adopted DLBCL gene expression datasets, Immune and stromal deconvolution, survival analysis on DLBCL datasets, and Visium spatial transcriptomics analysis is available in the Supplementary Methods.

Study approval

The human samples for the PDX model were collected and handled according to the Helsinki Declaration and the study was approved by the University of Palermo Ethical Review Board (approval numbers 09/2018 and 04/2023). Use of patient samples from National University Hospital, Singapore, was approved by NHG DSRB (Ref: 2015/00176; Title: SINGAPORE Lymphoproliferative Disease STUDY).

All animal experiments were conducted in compliance with institutional and national ethical guidelines. Studies involving Aicda$^{tm1(cre)Mnz/J}$ mice were approved by the Animal Welfare Organization (OPBA) of Palermo and by the Italian Ministry of Health, and were carried out in accordance with Italian legislation (D.lgs 26/2014; authorization number 495/2020-PR).

Experiments involving ATR inhibitor–treated animals were approved by IACUC (Ref: #181412 and #231766 from BRC, A*STAR).

Data Availability

All data generated in the present work have been made publicly available. The DSP data relative to 11 profiled DLBCL ROIs have been reported in Supplementary Table 4. The human bulk RNA-seq fastq files have been deposited in Sequence Read Archive (SRA) under accession codes PRJNA1082634, while the read counts have been reported in the Supplementary Table 10. The raw and processed data of Visium Spatial transcriptomics have been deposited in GEO under the accession code GSE260998. The DSP RNA-seq data profiled on tonsil GC DZ and LZ ROIs are publicly available(21). Values for all data points in graphs are reported in the Supporting Data Values file.

ACKNOWLEDGEMENTS

We thank S. Minardi (IFOM facility) for technical assistance with sequencing of Visium libraries.
This study was supported by the Italian Association for Cancer Research (AIRC; IG #22145 and AIRC; Accelerator Award #24296 to CT; AIRC; IG #23747 to SC; AIRC; IG#21366 to GS); the Italian Ministry of Education, University and Research (PRIN #2017K7FSYB and BIALYMP_eranetTRANSCAN3 to CT); the Singapore Ministry of Health's National Medical Research Council (Clinician Scientist Award MOH-000715-00 to ADJ); the National Institutes of Health–National Cancer Institute (R01CA242069 to LC); and the ERAPERMED2021-330 (GA 779282 to SS). CT and SC also acknowledge the MUR for the financial support under the project CN00000041 — National Center for Gene Therapy and Drugs based on RNA Technology, CUP B63C22000610006, Mission 4 Component 2 (M4C2), Investment 1.4 [CN3], SPOKE 2, Lot 5 of the National Recovery and Resilience Plan (PNRR) funded by the European Union "Next Generation EU". Additional support was provided by the project SCALE UP - Department of Excellence 2023–2027, funded by the Italian Ministry of University and Research to the Department of Molecular Biotechnology and Translational Medicine, University of Milan (to SC). G. Bertolazzi was supported by the Italian Ministry of Education, University and Research (MIUR) through the "PON Research and Innovation 2014–2020" until August 2024.

CONFLICT OF INTERESTS

ADJ has received consultancy fees from DKSH/Beigene, Roche, Gilead, Turbine Ltd, AstraZeneca, Antengene, Janssen, MSD and IQVIA; and research funding from Janssen and AstraZeneca.

AUTHOR CONTRIBUTIONS

VC, GB, ASYC. are co-first authors, with V.C. listed first as she initiated the project.
VC, GB, ASYC, SC, ADJ and CT designed the research studies. VC, GB, ASYC, GM, GB, GM, DP, CL, HL, GS, FM, MVR, FN, LB, ADN, IC, SV, GC, DV, BB, ML, ML, MSNO, ZB, TS, and EM conducted the experiments and analyzed data. PWJ, GS, SS, KPL, GV, MPC, SB, GI, LC, MF, SC, ADJ, CT and supervised the experiments and acquired data. SS, LC, SC, ADJ and CT acquired funding. VC, GB, ASYC, GM, GB, GM, DP, CL, HL, GS, PWJ, GS, FM, SP, MVR, FN, FP, SV, SS, ADN, SL, LL, AJMF, BB, GV, MPC, SB, GI, LC, MP, RZ, EM, JB, FF, MF, SC, ADJ and CT discussed and interpreted the results. VC, GB, ASYC, GM SC, ADJ and CT wrote the manuscript.CT, ADJ and SC are co-last authors, with CT listed last as he conceptualized the study.

FIGURE LEGENDS:

Figure 1

Spatial profiling uncovers unique transcriptional programs in the dark and light zones of germinal centers.

A, Representative IHC/IF micrographs showing Ki-67 (green signal), NGFR (pink signal), CD4 (blue signal), and CD8 (brown signal) expression. Ki-67 highlights proliferative DZ regions; NGFR marks the LZ. Original magnification, x200. Scale bar, 100 μm. **B,** Representative IF images of $CD3^+$ (green signal) and AID^+ (red signal) cells within GCs. Original magnification, x200. Scale bar, 100 μm. **C,** Cumulative distribution functions (CDFs) of $CD3^+$-AID^+ nearest-neighbor distances in observed samples (pink curve) versus randomized controls (black curve). Statistical analysis: Wilcoxon test. **D,** CDFs of $CD68^+$-AID^+ nearest-neighbor distances in observed versus randomized samples. Statistical analysis: Wilcoxon test. **E,** DSP analysis of ROIs from DZ (*n* = 5) and LZ (*n* = 5) regions defined by CD20 and NGFR expression. **F,** Volcano plot showing differentially expressed genes (adjusted $p < 0.05$) between DZ and LZ regions. **G,** Heatmap of DEGs with unsupervised hierarchical clustering across ROIs. **H,** Pathway enrichment of 169 DZ-upregulated genes using the Reactome Pathway database. **I,** Pathway enrichment of 201 LZ-upregulated genes using Reactome.

Figure 2

T-cell Distribution in the GC Varies by Subset and Function

A, Schematic overview of the CosMx SMI whole-transcriptome (WTX) workflow. FFPE tonsil tissues were processed, followed by immunofluorescence imaging and single-cell segmentation. Spatial transcriptomics was performed for 18,935 RNA targets, detecting approximately 900–1,100 transcripts per cell. Data were visualized by UMAP, and cell type identities were assigned via label transfer from the HCA tonsil reference dataset. **B,** Spatial enrichment maps of DZ and LZ transcriptional signatures across four representative GCs. **C,** Spatial distribution of T cell subtypes in GC microregions, highlighting immune cells including Tfh, CD8, Memory, Naïve CD8, Tregs, T-helper, γδT, Tfr, and DN cells. **D,** Quantification of T cell distribution relative to the DZ-LZ boundary. Cells were analyzed within a -100 μm (DZ) to 100 μm (LZ) range, binned into 10 μm increments. Subtypes analyzed include Treg, Tfh, CD8, Naïve CD4, Memory T, DN, and Naïve CD8, with spatial trends depicted in a line graph. **E,** Quantification of T cell subtypes including Tfh, Memory CD4, Memory CD8, DN, Naïve CD4, and Naïve CD8 cells based on Macsima hyperplex analyses to evaluate their differential distribution between DZ and LZ. (*n* GCs = 9). Statistical analysis was assessed using a two-tailed unpaired Mann-Whitney test. Values are shown as mean ± standard error; *, $P < 0.05$. **F,** Volcano plot of differentially expressed genes between DZ and LZ B cells, highlighting upregulated genes in each region (adj.p-value < 0.05). **G,** Heatmap of HLA class I and II gene expression in DZ versus LZ regions, clustered hierarchically by expression pattern.

Figure 3

The GC DZ spatial signature in aggressive B cell lymphomas is associated with reduced T cell infiltration.

A, DZ enrichment scores correlating DZ gene expression and xCell T-cell cytotype scores calculated in 8 DLBCL datasets. Positive DZ enrichment values indicate a positive association between the DZ spatial signature and the xCell cytotype scores, while negative values indicate

a negative association. Statistical significance is shown with Wilcoxon adjusted p-values. **B,** UMAP projection of 1078 harmonized DLBCL cases classified based on the DZ/LZ spatial signature; DZ-like cases (red), LZ-like cases (light blue), intermediate cases (green). **C,** Kaplan-Meier survival plot showing overall survival of DZ-like, LZ-like, and intermediate groups from the harmonized dataset (1078 cases). **D,** Digital spatial profiling images of 11 ROIs selected within CD20 (green signal) and CD3E (red signal) infiltrates of a lymph node with DLBCL. Total expression of the DZ signature is shown from low (pink) to high (red). Original magnification, x50. Scale bar, 250 µm.

E, Pie charts showing SpatialDecon cytotype scores across 11 ROIs, ranked by DZ signature expression. **F,** Scatter plot with correlation line of DZ spatial signature expression and SpatialDecon T-cell score across 11 ROIs (Kendall's correlation, p-value < 0.05). **G,** DSP images of lowest DZ signature expression ROI (001) and the highest DZ signature expression ROI (004). **H,** Schematic of DLBCL tissue microarray (TMA) consisting of 103 patient samples, analyzed using DSP WTA with DAPI, CD20 (red signal) and CD3E (cyan signal) to observe T cell content and DZ signature expression. **I,** Box plot comparing CD3 AOI nuclear count percentages between high and low DZ signature groups. Statistical analysis was performed using a two-tailed unpaired Mann-Whitney test. Values are shown as mean ± standard error; ****, P < 0.0001.

J, Scatter plot with correlation line of DZ spatial signature expression within the $CD20^+$ segment and the percentage of $CD3^+$ cells per ROI across 79 DLBCL samples. Statistical significance was assessed using spearman correlation coefficient (R) and p-value.

Figure 4

The spatial signature of DZ cells is independent of AICDA-related mutational processes.

A, Representative microphotographs of H&E and IHC for Cre^+ and Ki-67^+ cells on mesenteric lymph nodes from WT and *Aicda*$^{-/-}$ mice. Original magnification, x200. Scale bar, 100 µm. **B-C,** Quantitative analyses of Cre^+ (**B**) and Ki-67^+ (**C**) cells in WT and *Aicda*$^{-/-}$ GCs (*n* = 20). Statistical analysis was assessed using a two-tailed unpaired Mann-Whitney test. Values are shown as mean ± standard error; ***, P < 0.001; ****, P < 0.0001. **D,** Representative microphotographs of H&E-stained sections from WT and *Aicda*$^{-/-}$ mesenteric lymph nodes involved in the Visium spatial transcriptome experiment profiling. Original magnification, x50. Scale bar, 250 µm. **E**, Spatial visualization of WT and *Aicda*$^{-/-}$ follicle/GC clusters. **F,** Volcano plot showing differentially expressed genes between WT cluster 4 and *Aicda*$^{-/-}$ clusters 1 and 3 (Wilcoxon Rank Sum test adj. p-values < 0.05, abs-logFC > 0.025). **G-H,** Spatial projection of the DZ spatial signature (**G**) and T-cell signature (**H**) total expression in WT and *Aicda*$^{-/-}$ samples. **I-L,** Representative microphotographs of triple immunohistochemical staining for DZ Ki-67^+ (cyan signal), LZ $CD21^+$ (pink signal) and $CD4^+$ (**I**) or $CD8^+$ cells (**K**) (brown signal) and quantitative analyses of the percentage of $CD4^+$ (**J**) or $CD8^+$ (**L**) T cells in WT and *Aicda*$^{-/-}$ GCs. (*n* = 10 WT GCs; *n* = 10 *Aicda*$^{-/-}$ GCs). Original magnifications x400. Scale bar, 50 µm. Statistical analysis: two-tailed unpaired Mann-Whitney test. Mean ± standard error shown. **M,** GSEA enrichment analysis of DZ spatial signature in AICDA-high and AICDA-low DZ B-cells. **N,** Pathway enrichment of 257 *AICDA*-high signature genes using Reactome Pathway library. **O,** Pathway enrichment of 127 *AICDA*-low signature genes using Reactome Pathway library.

Figure 5

ATRi allows immune permeation of a DZ-like DLBCL in-vitro

A, Schematic of ATR inhibitor (Ceralasertib, AZD6738) treatment in HT and SUDHL-5 cells. Cells were treated with DMSO or AZD6738 at 1μM for 48 hours. **B,** Representative immunofluorescence images of HT and SUDHL-5 nuclei after treatment with 1μM ATR inhibitor for 48h (green: laminB1)**.** Arrows point to micronuclei. **C,** Quantification of micronuclei formation (relative to IF analysis **B**). **D,** GSEA enrichment analysis on ATRi and DMSO samples using the MHC and IFNγ signature. **E,** GSEA enrichment analysis on ATRi and DMSO samples using the DZ and LZ spatial signature. **F,** Schematic of the competitive device. PKH26-labeled PBMCs were loaded in the central fluidic chamber. DLBCL (HT or SUDHL-5) cells were embedded in Matrigel with ATRi or DMSO and loaded in lateral chambers. **G-J,** Visualization and quantification of red fluorescent PBMCs in HT (**G,H**) and SUDHL-5 (**I,J**) cell chambers measured at 24h and 48h. Mean of representative fields ± S.D. from 3 replicates of different donor PBMCs (*n* = 3) is shown. **K,** Confocal microscopy of cells in ATRi-treated DLBCL-gel chamber at the 48h time point. Arrows point to interactions between $CD3^+$ (green signal) $PKH26^+$ (red signal) T cells and DAPI (blue signal) HT cells. Both visible light image (left panel) and Z-stack acquisition (right panel) are shown. **L,** Box plot of distances between PBMCs and tumor cells in DMSO and ATRi chambers of the microfluidic chip measured via X, Y, and Z coordinates from the microfluidic chip. **M,** Schematic representation of the experimental protocol. Primary tumor cells isolated from DLBCL patient-derived xenografts (PDX) were selected based on their spatial gene expression profiles, classified as DZ-like or LZ-like. Tumor cells pretreated with the ATR inhibitor AZD6738 (1 μM or 5 μM) were used in T-cell-mediated cytotoxicity assays. **N-O,** Dose-response curve of T-cell mediated killing across indicated target:effector ratios of DZ-like (**N**) or LZ-like (**O**) DLBCL PDX-derived cells treated with 1 or 5μM ATRi.
Statistical analysis was assessed using a two-tailed unpaired Mann-Whitney test (**C, H, J, L**). Values are shown as mean ± standard error; *, $P < 0.05$; **, $P < 0.01$; ****, $P < 0.0001$.

Figure 6
Functional impact of ATRi treatment on the GC response
A, Schematic representation of the experimental protocol. In one experiment on ten C57BL/6J mice, immunization with NP-OVA in alum on Day 0, followed by treatment with vehicle (*n* = 5) or AZD6738 (50 mg/kg, *n* = 5) was performed from Day 2 to Day 6. Mesenteric lymph nodes (mLNs) were harvested on Day 7 for analysis. **B,** Box plots showing quantitative analysis of $CD3^+$, $CD4^+$, and $CD8^+$ T-cell infiltration in indicated number of total GCs, DZ, and LZ compartments in vehicle (CTRL) versus ATRi-treated mice. **C,** Representative microphotographs of double-marker IHC for Ki-67^+ (brown signal) and $CD3^+$ (pink signal) cells in mLN GCs from vehicle (CTRL) and ATRi-treated mice. Original magnifications x400. Scale bar, 50 μm. **D,** Combined IHC/IF staining for $CD3^+$ (brown signal), $CD21^+$ (pink signal), and Ki-67^+ (cyan signal) cells in mLN GCs from vehicle (CTRL) and ATRi-treated mice, showing the spatial distribution of T cells in the DZ and LZ compartments. Original magnifications x400. Scale bar, 50 μm. **E,** Combined IHC/IF staining for $CD4^+$ (pink signal), $CD8^+$ (brown signal) and Ki-67^+ (cyan signal) cells in mLN GCs from vehicle (CTRL) and ATRi-treated mice, illustrating the phenotype of infiltrating T cells. Original magnifications x400. Scale bar, 50 μm. **F,** Box plots showing quantitative analysis of *Ifnγ*$^+$$CD8^+$ T cells, *Ifnb1*$^+$$CD20^+$ B cells, and MHC-I expression in indicated number of total GCs, DZ, and LZ compartments in vehicle (CTRL) versus ATRi-treated mice. **G,** Representative images of combined mRNA *in situ* hybridization for *Ifnγ* (brown signal) and double-marker IHC for CD8 (pink signal) and Ki-67 (cyan signal) in mLN GCs from vehicle (CTRL) and ATRi-treated mice, showing the localization of activated

$CD8^+$ T cells. Original magnifications x400 and x630 (insets). Scale bar, 50 μm and 25 μm. **H,** Representative images of combined mRNA *in situ* hybridization for *Ifnb1* (brown signal) and double-marker IHC for CD20 (pink signal) and Ki-67 (cyan signal) in vehicle (CTRL) and ATRi-treated mice, highlighting the induction of type I interferon response in the DZ. Original magnifications x400 and x630 (insets). Scale bar, 50 μm and 25 μm. **I,** Representative immunohistochemical staining for MHC-I (brown signal) or MHC-I (brown signal) and Ki-67 (violet signal) in vehicle (CTRL) and ATRi-treated mice, demonstrating increased MHC-I expression in the DZ in response to ATR inhibition. Original magnifications x400 and x630 (insets). Scale bar, 50 μm and 25 μm.
Box plots statistical analysis: two-tailed unpaired Mann-Whitney test. Mean ± standard error shown; *, $P < 0.05$; **, $P < 0.01$, ***, $P < 0.001$.

REFERENCE

1. Galassi C, et al. The hallmarks of cancer immune evasion. *Cancer Cell*. 2024;42(11):1825–1863.

2. Robert C. A decade of immune-checkpoint inhibitors in cancer therapy. *Nature Communications*. 2020;11(1):1–3.

3. Togashi Y, Shitara K, Nishikawa H. Regulatory T cells in cancer immunosuppression - implications for anticancer therapy. *Nat Rev Clin Oncol*. 2019;16(6):356–371.

4. Veglia F, Sanseviero E, Gabrilovich DI. Myeloid-derived suppressor cells in the era of increasing myeloid cell diversity. *Nat Rev Immunol*. 2021;21(8):485–498.

5. Sangaletti S, et al. Mesenchymal Transition of High-Grade Breast Carcinomas Depends on Extracellular Matrix Control of Myeloid Suppressor Cell Activity. *Cell Rep*. 2016;17(1):233–248.

6. Frittoli E, et al. Tissue fluidification promotes a cGAS-STING cytosolic DNA response in invasive breast cancer. *Nat Mater*. 2023;22(5):644–655.

7. Grout JA, et al. Spatial Positioning and Matrix Programs of Cancer-Associated Fibroblasts Promote T-cell Exclusion in Human Lung Tumors. *Cancer Discov*. 2022;12(11):2606–2625.

8. Jenkins L, et al. Cancer-Associated Fibroblasts Suppress CD8+ T-cell Infiltration and

Confer Resistance to Immune-Checkpoint Blockade. *Cancer Res*. 2022;82(16):2904–2917.

9. Mariathasan S, et al. TGFβ attenuates tumour response to PD-L1 blockade by contributing to exclusion of T cells. *Nature*. 2018;554(7693):544–548.

10. Collins NB, et al. PI3K activation allows immune evasion by promoting an inhibitory myeloid tumor microenvironment. *J Immunother Cancer*. 2022;10(3). https://doi.org/10.1136/jitc-2021-003402.

11. Luke JJ, et al. WNT/β-catenin Pathway Activation Correlates with Immune Exclusion across Human Cancers. *Clin Cancer Res*. 2019;25(10):3074–3083.

12. de Charette M, Houot R. Hide or defend, the two strategies of lymphoma immune evasion: potential implications for immunotherapy. *Haematologica*. 2018;103(8):1256–1268.

13. Curran EK, Godfrey J, Kline J. Mechanisms of Immune Tolerance in Leukemia and Lymphoma. *Trends Immunol*. 2017;38(7):513–525.

14. Ennishi D, et al. Double-Hit Gene Expression Signature Defines a Distinct Subgroup of Germinal Center B-Cell-Like Diffuse Large B-Cell Lymphoma. *J Clin Oncol*. 2019;37(3):190–201.

15. Urata T, et al. Distribution and clinical impact of molecular subtypes with dark zone signature of DLBCL in a Japanese real-world study. *Blood Adv*. 2023;7(24):7459–7470.

16. Victora GD, et al. Identification of human germinal center light and dark zone cells and their relationship to human B-cell lymphomas. *Blood*. 2012;120(11):2240–2248.

17. Holmes AB, et al. Single-cell analysis of germinal-center B cells informs on lymphoma cell of origin and outcome. *J Exp Med*. 2020;217(10). https://doi.org/10.1084/jem.20200483.

18. Tripodo C, et al. A Spatially Resolved Dark- versus Light-Zone Microenvironment Signature Subdivides Germinal Center-Related Aggressive B Cell Lymphomas. *iScience*.

2020;23(10):101562.

19. Victora GD, et al. Germinal center dynamics revealed by multiphoton microscopy with a photoactivatable fluorescent reporter. *Cell*. 2010;143(4):592–605.

20. Stebegg M, et al. Regulation of the Germinal Center Response. *Front Immunol*. 2018;9:2469.

21. L'Imperio V, et al. Spatial transcriptome of a germinal center plasmablastic burst hints at MYD88/CD79B mutants-enriched diffuse large B-cell lymphomas. *Eur J Immunol*. 2022;52(8):1350–1361.

22. Massoni-Badosa R, et al. An atlas of cells in the human tonsil. *Immunity*. 2024;57(2):379–399.e18.

23. Kalyan S, Kabelitz D. Defining the nature of human γδ T cells: a biographical sketch of the highly empathetic. *Cell Mol Immunol*. 2013;10(1):21–29.

24. Barrans SL, et al. Whole genome expression profiling based on paraffin embedded tissue can be used to classify diffuse large B-cell lymphoma and predict clinical outcome. *Br J Haematol*. 2012;159(4):441–453.

25. Chapuy B, et al. Molecular subtypes of diffuse large B cell lymphoma are associated with distinct pathogenic mechanisms and outcomes. *Nat Med*. 2018;24(5):679–690.

26. Dubois S, et al. Biological and Clinical Relevance of Associated Genomic Alterations in MYD88 L265P and non-L265P-Mutated Diffuse Large B-Cell Lymphoma: Analysis of 361 Cases. *Clin Cancer Res*. 2017;23(9):2232–2244.

27. Lenz G, et al. Stromal gene signatures in large-B-cell lymphomas. *N Engl J Med*. 2008;359(22):2313–2323.

28. Reddy A, et al. Genetic and Functional Drivers of Diffuse Large B Cell Lymphoma. *Cell*.

2017;171(2):481–494.e15.

29. Schmitz R, et al. Genetics and Pathogenesis of Diffuse Large B-Cell Lymphoma. *N Engl J Med*. 2018;378(15):1396–1407.

30. Sha C, et al. Molecular High-Grade B-Cell Lymphoma: Defining a Poor-Risk Group That Requires Different Approaches to Therapy. *J Clin Oncol*. 2019;37(3):202–212.

31. Visco C, et al. Comprehensive gene expression profiling and immunohistochemical studies support application of immunophenotypic algorithm for molecular subtype classification in diffuse large B-cell lymphoma: a report from the International DLBCL Rituximab-CHOP Consortium Program Study. *Leukemia*. 2012;26(9):2103–2113.

32. Aran D, Hu Z, Butte AJ. xCell: digitally portraying the tissue cellular heterogeneity landscape. *Genome Biol*. 2017;18(1):220.

33. Liu M, et al. Spatially-resolved transcriptomics reveal macrophage heterogeneity and prognostic significance in diffuse large B-cell lymphoma. *Nat Commun*. 2024;15(1):2113.

34. Teater M, et al. AICDA drives epigenetic heterogeneity and accelerates germinal center-derived lymphomagenesis. *Nat Commun*. 2018;9(1):222.

35. Robbiani DF, et al. AID is required for the chromosomal breaks in c-myc that lead to c-myc/IgH translocations. *Cell*. 2008;135(6):1028–1038.

36. Muramatsu M, et al. Class switch recombination and hypermutation require activation-induced cytidine deaminase (AID), a potential RNA editing enzyme. *Cell*. 2000;102(5):553–563.

37. Kidiyoor GR, et al. ATR is essential for preservation of cell mechanics and nuclear integrity during interstitial migration. *Nat Commun*. 2020;11(1):4828.

38. Kidiyoor GR, Kumar A, Foiani M. ATR-mediated regulation of nuclear and cellular

plasticity. *DNA Repair (Amst)*. 2016;44:143–150.

39. Kumar A, et al. ATR mediates a checkpoint at the nuclear envelope in response to mechanical stress. *Cell*. 2014;158(3):633–646.

40. Venkatachalapathy S, Jokhun DS, Shivashankar GV. Multivariate analysis reveals activation-primed fibroblast geometric states in engineered 3D tumor microenvironments. *Mol Biol Cell*. 2020;31(8):803–812.

41. Mackenzie KJ, et al. cGAS surveillance of micronuclei links genome instability to innate immunity. *Nature*. 2017;548(7668):461–465.

42. Lucarini V, et al. Combining Type I Interferons and 5-Aza-2'-Deoxycitidine to Improve Anti-Tumor Response against Melanoma. *J Invest Dermatol*. 2017;137(1):159–169.

43. Musella M, et al. Type I IFNs promote cancer cell stemness by triggering the epigenetic regulator KDM1B. *Nat Immunol*. 2022;23(9):1379–1392.

44. Davies JR, et al. Comparison of MHG and DZsig reveals shared biology and a core overlap group with inferior prognosis in DLBCL. *Blood Adv*. 2023;7(20):6156–6162.

45. Dickinson MJ, et al. Glofitamab for Relapsed or Refractory Diffuse Large B-Cell Lymphoma. *N Engl J Med*. 2022;387(24):2220–2231.

46. Taniguchi H, et al. ATR inhibition activates cancer cell cGAS/STING-interferon signaling and promotes antitumor immunity in small-cell lung cancer. *Sci Adv*. 2024;10(39):eado4618.

47. Patin EC, et al. Sculpting the tumour microenvironment by combining radiotherapy and ATR inhibition for curative-intent adjuvant immunotherapy. *Nat Commun*. 2024;15(1):6923.

48. Hardaker EL, et al. The ATR inhibitor ceralasertib potentiates cancer checkpoint immunotherapy by regulating the tumor microenvironment. *Nat Commun*. 2024;15(1):1700.

49. Fiore D, et al. A patient-derived T cell lymphoma biorepository uncovers pathogenetic

mechanisms and host-related therapeutic vulnerabilities. *Cell Rep Med*. 2025;6(4):102029.

50. Businaro L, et al. Cross talk between cancer and immune cells: exploring complex dynamics in a microfluidic environment. *Lab Chip*. 2013;13(2):229–239.

51. Kinkhabwala A, et al. MACSima imaging cyclic staining (MICS) technology reveals combinatorial target pairs for CAR T cell treatment of solid tumors. *Sci Rep*. 2022;12(1):1911.

52. Tripodo C, et al. Stromal SPARC contributes to the detrimental fibrotic changes associated with myeloproliferation whereas its deficiency favors myeloid cell expansion. *Blood*. 2012;120(17):3541–3554.

53. Ritchie ME, et al. limma powers differential expression analyses for RNA-sequencing and microarray studies. *Nucleic Acids Res*. 2015;43(7):e47.

54. Yu G, He Q-Y. ReactomePA: an R/Bioconductor package for reactome pathway analysis and visualization. *Mol Biosyst*. 2016;12(2):477–479.

55. SpatialDecon: Deconvolution of mixed cells from spatial and/or bulk gene expression data [Internet]. 2020. https://rdrr.io/bioc/SpatialDecon/. Accessed June 9, 2025.

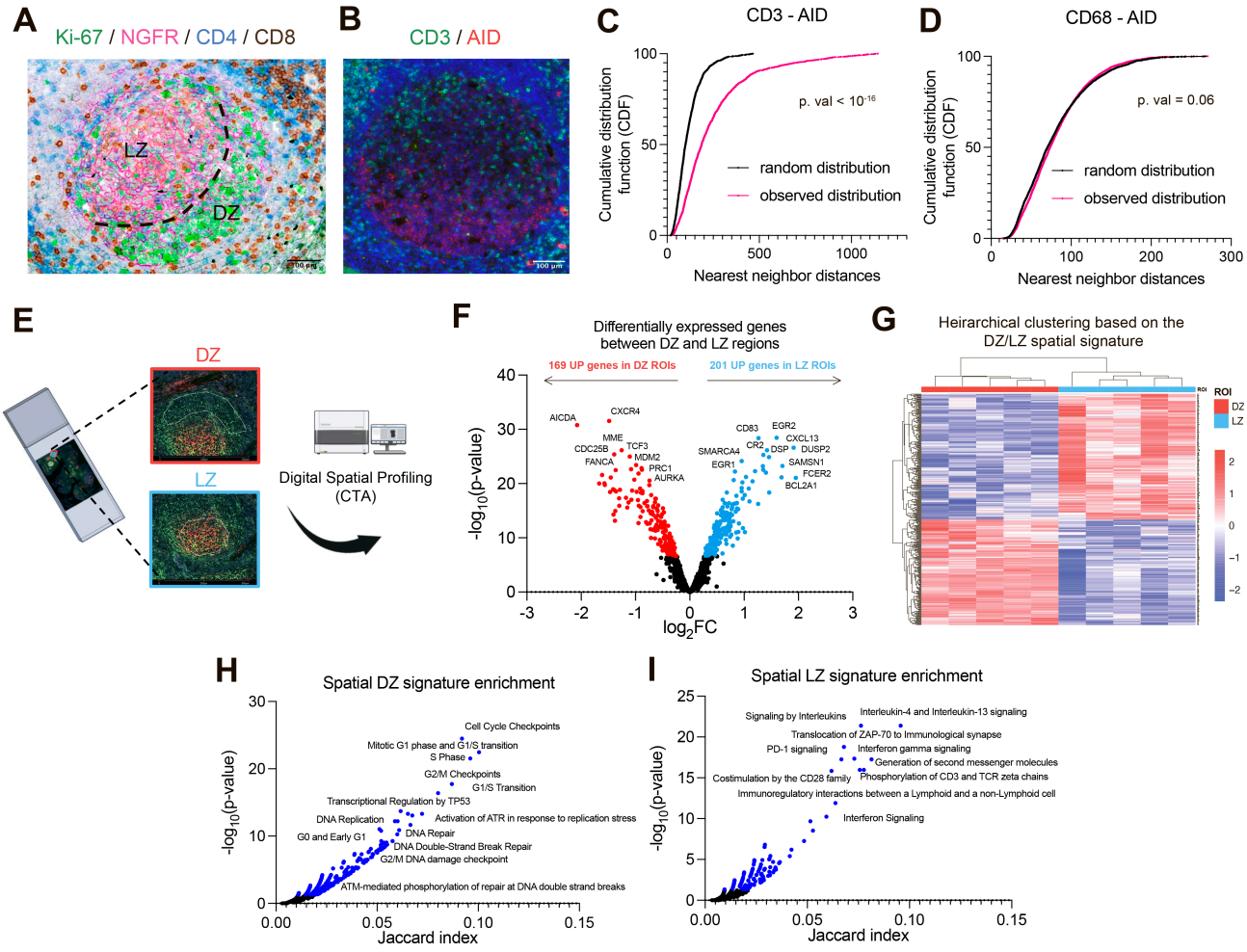
A
Ki-67 / NGFR / CD4 / CD8
LZ
DZ
B
CD3 / AID
C
CD3 - AID
Cumulative distribution function (CDF)
p. val < 10-16
random distribution
observed distribution
Nearest neighbor distances
D
CD68 - AID
p. val = 0.06
E
DZ
LZ
Digital Spatial Profiling (CTA)
F
Differentially expressed genes between DZ and LZ regions
169 UP genes in DZ ROIs
201 UP genes in LZ ROIs
-log10(p-value)
log2FC
AICDA
CXCR4
MME
CDC25B
TCF3
MDM2
FANCA
PRC1
AURKA
CD83
EGR2
CR2
CXCL13
DSP
DUSP2
SMARCA4
EGR1
SAMSN1
FCER2
BCL2A1
G
Heirarchical clustering based on the DZ/LZ spatial signature
ROI
DZ
LZ
H
Spatial DZ signature enrichment
-log10(p-value)
Jaccard index
Cell Cycle Checkpoints
Mitotic G1 phase and G1/S transition
S Phase
G2/M Checkpoints
G1/S Transition
Transcriptional Regulation by TP53
DNA Replication
Activation of ATR in response to replication stress
G0 and Early G1
DNA Repair
DNA Double-Strand Break Repair
G2/M DNA damage checkpoint
ATM-mediated phosphorylation of repair at DNA double strand breaks
I
Spatial LZ signature enrichment
-log10(p-value)
Jaccard index
Signaling by Interleukins
Interleukin-4 and Interleukin-13 signaling
Translocation of ZAP-70 to Immunological synapse
PD-1 signaling
Interferon gamma signaling
Generation of second messenger molecules
Costimulation by the CD28 family
Phosphorylation of CD3 and TCR zeta chains
Immunoregulatory interactions between a Lymphoid and a non-Lymphoid cell
Interferon Signaling

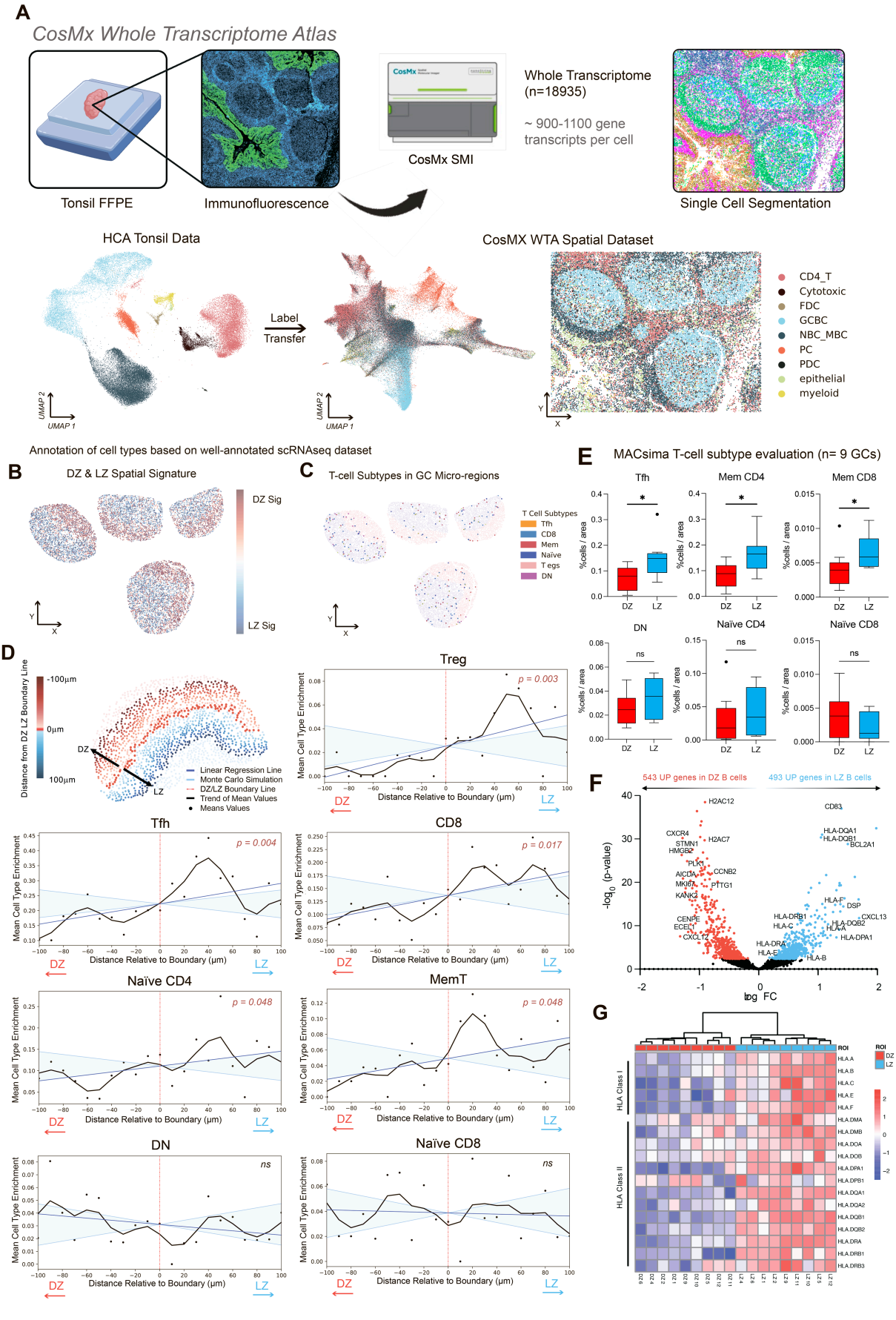
A
CosMx Whole Transcriptome Atlas
Tonsil FFPE
Immunofluorescence
CosMx SMI
Whole Transcriptome
(n=18935)
~ 900-1100 gene
transcripts per cell
Single Cell Segmentation
HCA Tonsil Data
Label
Transfer
CosMX WTA Spatial Dataset
CD4_T
Cytotoxic
FDC
GCBC
NBC_MBC
PC
PDC
epithelial
myeloid
UMAP 1
UMAP 2
Annotation of cell types based on well-annotated scRNAseq dataset
B
DZ & LZ Spatial Signature
DZ Sig
LZ Sig
C
T-cell Subtypes in GC Micro-regions
T Cell Subtypes
Tfh
CD8
Mem
Naïve
T egs
DN
D
Distance from DZ LZ Boundary Line
-100µm
0µm
100µm
DZ
LZ
Linear Regression Line
Monte Carlo Simulation
DZ/LZ Boundary Line
Trend of Mean Values
Means Values
Treg
p = 0.003
Tfh
p = 0.004
CD8
p = 0.017
Naïve CD4
p = 0.048
MemT
p = 0.048
DN
ns
Naïve CD8
ns
Mean Cell Type Enrichment
Distance Relative to Boundary (µm)
E
MACsima T-cell subtype evaluation (n= 9 GCs)
Tfh
Mem CD4
Mem CD8
DN
Naïve CD4
Naïve CD8
%cells / area
ns
F
543 UP genes in DZ B cells
493 UP genes in LZ B cells
-log10 (p-value)
log FC
G
ROI
HLA Class I
HLA Class II
HLA.A
HLA.B
HLA.C
HLA.E
HLA.F
HLA.DMA
HLA.DMB
HLA.DOA
HLA.DOB
HLA.DPA1
HLA.DPB1
HLA.DQA1
HLA.DQA2
HLA.DQB1
HLA.DQB2
HLA.DRA
HLA.DRB1
HLA.DRB3

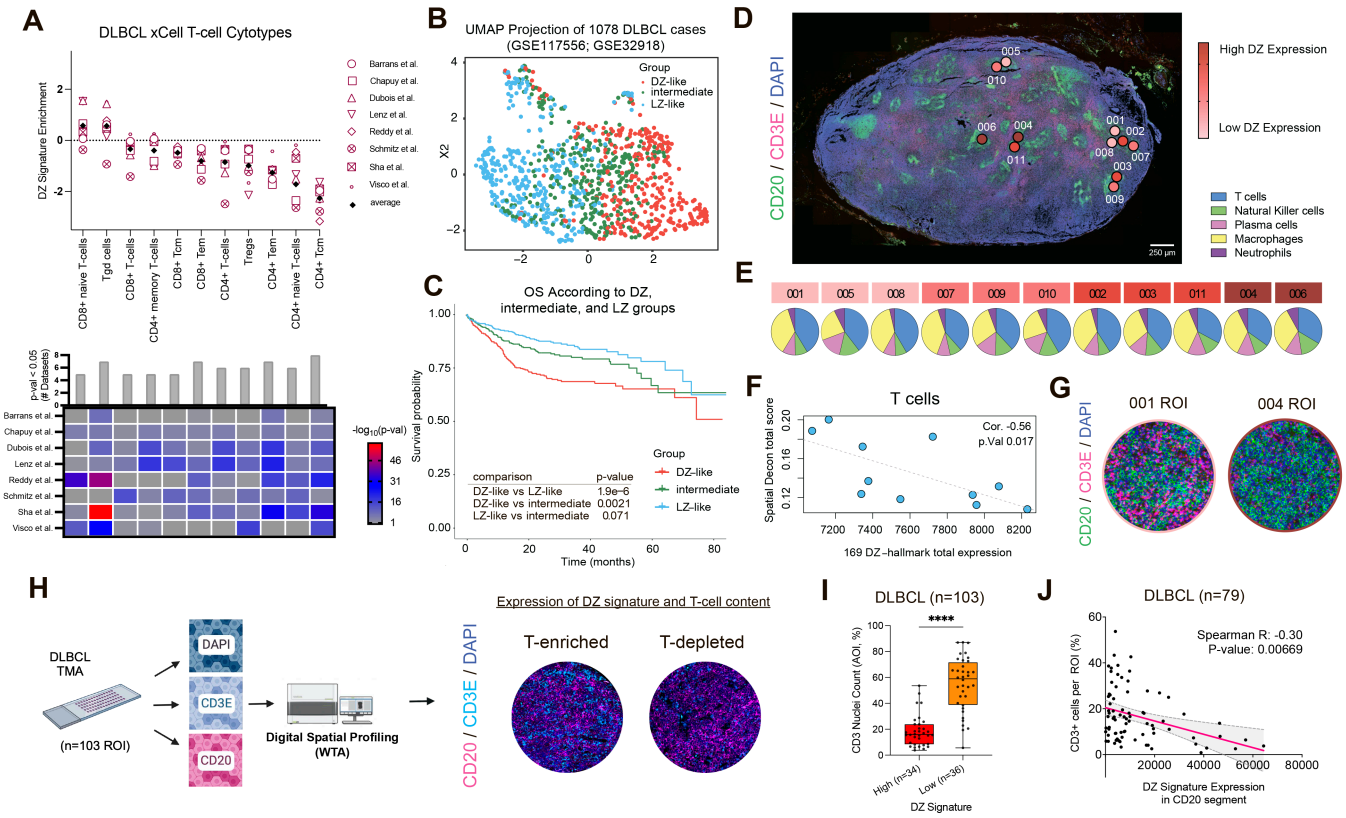
A
DLBCL xCell T-cell Cytotypes
DZ Signature Enrichment
CD8+ naive T-cells
Tgd cells
CD8+ T-cells
CD4+ memory T-cells
CD8+ Tcm
CD8+ Tem
CD4+ T-cells
Tregs
CD4+ Tem
CD4+ naive T-cells
CD4+ Tcm
Barrans et al.
Chapuy et al.
Dubois et al.
Lenz et al.
Reddy et al.
Schmitz et al.
Sha et al.
Visco et al.
average
p-val < 0.05 (# Datasets)
-log10(p-val)
B
UMAP Projection of 1078 DLBCL cases (GSE117556; GSE32918)
Group
DZ-like
intermediate
LZ-like
C
OS According to DZ, intermediate, and LZ groups
Survival probability
Time (months)
comparison p-value
DZ-like vs LZ-like 1.9e−6
DZ-like vs intermediate 0.0021
LZ-like vs intermediate 0.071
D
CD20 / CD3E / DAPI
High DZ Expression
Low DZ Expression
T cells
Natural Killer cells
Plasma cells
Macrophages
Neutrophils
250 µm
E
001 005 008 007 009 010 002 003 011 004 006
F
T cells
Spatial Decon total score
Cor. -0.56
p.Val 0.017
169 DZ−hallmark total expression
G
001 ROI
004 ROI
CD20 / CD3E / DAPI
H
DLBCL TMA
(n=103 ROI)
DAPI
CD3E
CD20
Digital Spatial Profiling (WTA)
Expression of DZ signature and T-cell content
T-enriched
T-depleted
CD20 / CD3E / DAPI
I
DLBCL (n=103)
CD3 Nuclei Count (AOI, %)
****
High (n=34)
Low (n=36)
DZ Signature
J
DLBCL (n=79)
Spearman R: -0.30
P-value: 0.00669
CD3+ cells per ROI (%)
DZ Signature Expression in CD20 segment

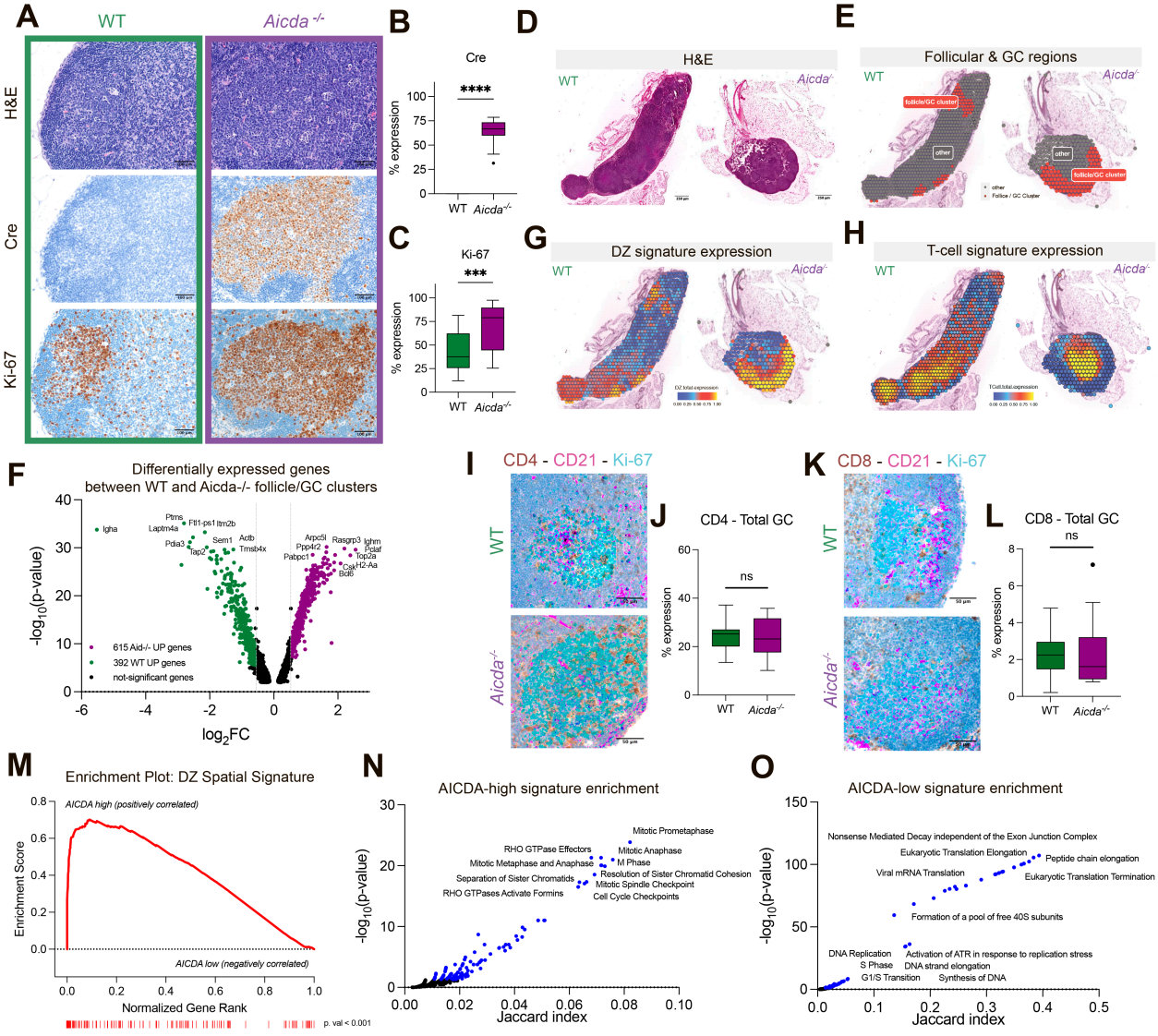
A
WT
Aicda -/-
H&E
Cre
Ki-67
B
Cre
****
% expression
WT
Aicda-/-
C
Ki-67
***
% expression
WT
Aicda-/-
D
H&E
WT
Aicda-/-
E
Follicular & GC regions
WT
Aicda-/-
follicle/GC cluster
other
G
DZ signature expression
WT
Aicda-/-
H
T-cell signature expression
WT
Aicda-/-
F
Differentially expressed genes
between WT and Aicda-/- follicle/GC clusters
-log10(p-value)
log2FC
615 Aid-/- UP genes
392 WT UP genes
not-significant genes
Igha
Ptms
Laptm4a
Fli1-ps1
Itm2b
Pdia3
Sem1
Actb
Tmsb4x
Tapt
Arpc5l
Ppp4r2
Pabpc1
Rasgrp3
Ighm
Pclaf
Top2a
Cd4
H2-Aa
Bcl6
I
CD4 - CD21 - Ki-67
WT
Aicda-/-
J
CD4 - Total GC
ns
% expression
WT
Aicda-/-
K
CD8 - CD21 - Ki-67
WT
Aicda-/-
L
CD8 - Total GC
ns
% expression
WT
Aicda-/-
M
Enrichment Plot: DZ Spatial Signature
AICDA high (positively correlated)
AICDA low (negatively correlated)
Enrichment Score
Normalized Gene Rank
p. val < 0.001
N
AICDA-high signature enrichment
-log10(p-value)
Jaccard index
Mitotic Prometaphase
RHO GTPase Effectors
Mitotic Anaphase
Mitotic Metaphase and Anaphase
M Phase
Separation of Sister Chromatids
Resolution of Sister Chromatid Cohesion
RHO GTPases Activate Formins
Mitotic Spindle Checkpoint
Cell Cycle Checkpoints
O
AICDA-low signature enrichment
-log10(p-value)
Jaccard index
Nonsense Mediated Decay independent of the Exon Junction Complex
Eukaryotic Translation Elongation
Peptide chain elongation
Viral mRNA Translation
Eukaryotic Translation Termination
Formation of a pool of free 40S subunits
DNA Replication
Activation of ATR in response to replication stress
S Phase
DNA strand elongation
G1/S Transition
Synthesis of DNA

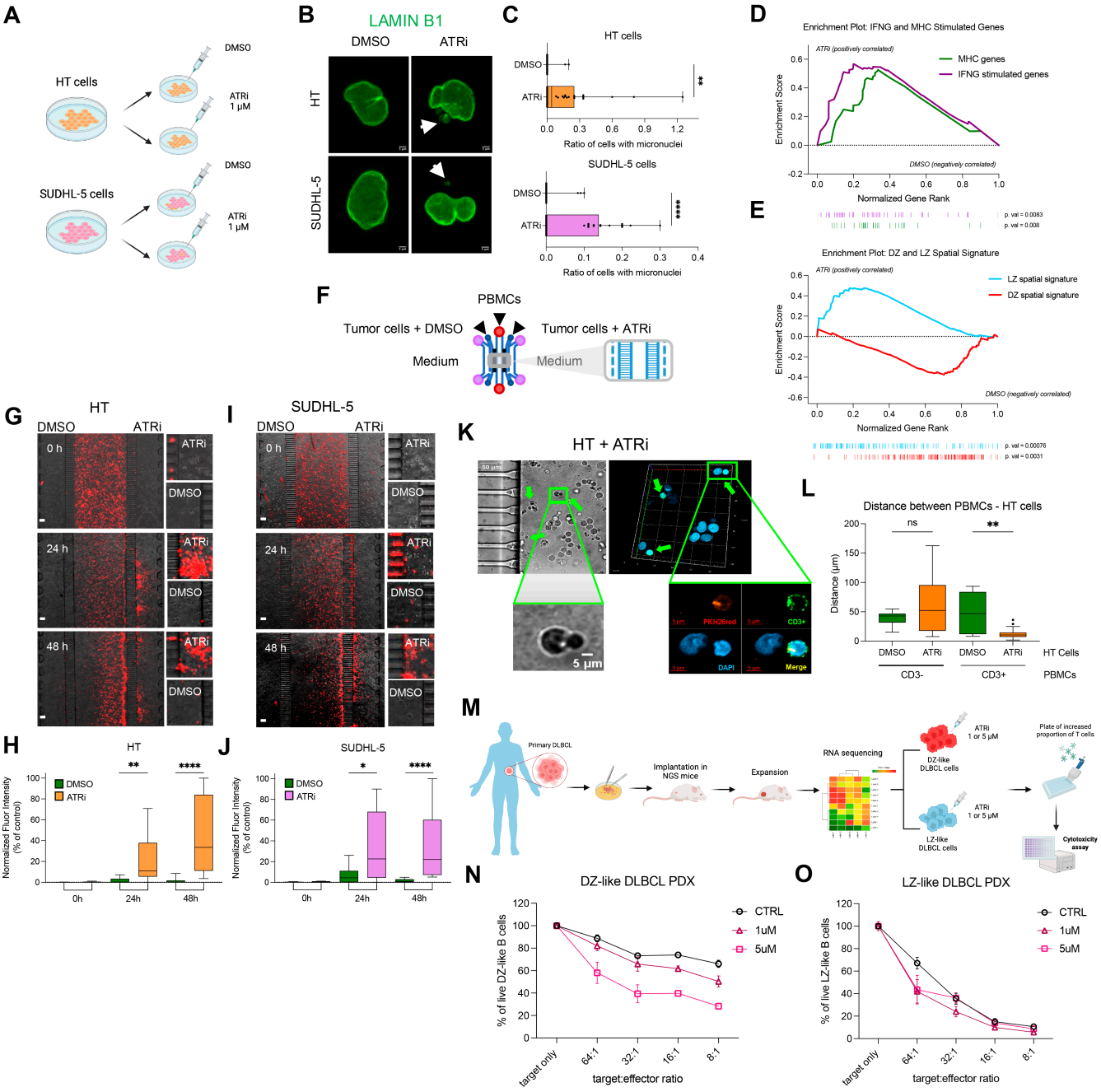
A
HT cells
DMSO
ATRi 1 μM
SUDHL-5 cells
DMSO
ATRi 1 μM
B
LAMIN B1
DMSO
ATRi
HT
SUDHL-5
C
HT cells
DMSO
ATRi
**
0.0 0.3 0.6 0.9 1.2
Ratio of cells with micronuclei
SUDHL-5 cells
DMSO
ATRi
****
0.0 0.1 0.2 0.3 0.4
Ratio of cells with micronuclei
D
Enrichment Plot: IFNG and MHC Stimulated Genes
ATRi (positively correlated)
MHC genes
IFNG stimulated genes
Enrichment Score
0.6 0.4 0.2 0.0 -0.2
DMSO (negatively correlated)
0.0 0.2 0.4 0.6 0.8 1.0
Normalized Gene Rank
E
p. val = 0.0083
p. val = 0.008
Enrichment Plot: DZ and LZ Spatial Signature
ATRi (positively correlated)
LZ spatial signature
DZ spatial signature
Enrichment Score
0.6 0.4 0.2 0.0 -0.2 -0.4 -0.6
DMSO (negatively correlated)
0.0 0.2 0.4 0.6 0.8 1.0
Normalized Gene Rank
p. val = 0.00076
p. val = 0.0031
F
PBMCs
Tumor cells + DMSO
Tumor cells + ATRi
Medium
Medium
G
HT
DMSO
ATRi
0 h
24 h
48 h
ATRi
DMSO
I
SUDHL-5
DMSO
ATRi
0 h
24 h
48 h
ATRi
DMSO
K
HT + ATRi
50 μm
5 μm
PKH26red
CD3+
DAPI
Merge
L
Distance between PBMCs - HT cells
ns
**
Distance (μm)
200 150 100 50 0
DMSO ATRi DMSO ATRi
HT Cells
CD3- CD3+
PBMCs
H
HT
**
****
Normalized Fluor Intensity (% of control)
100 80 60 40 20 0
DMSO
ATRi
0h 24h 48h
J
SUDHL-5
*
****
Normalized Fluor Intensity (% of control)
100 80 60 40 20 0
DMSO
ATRi
0h 24h 48h
M
Primary DLBCL
Implantation in NGS mice
Expansion
RNA sequencing
DZ-like DLBCL cells
LZ-like DLBCL cells
ATRi 1 or 5 μM
ATRi 1 or 5 μM
Plate of increased proportion of T cells
Cytotoxicity assay
N
DZ-like DLBCL PDX
% of live DZ-like B cells
120 100 80 60 40 20 0
CTRL
1uM
5uM
target only 64:1 32:1 16:1 8:1
target:effector ratio
O
LZ-like DLBCL PDX
% of live LZ-like B cells
120 100 80 60 40 20 0
CTRL
1uM
5uM
target only 64:1 32:1 16:1 8:1
target:effector ratio

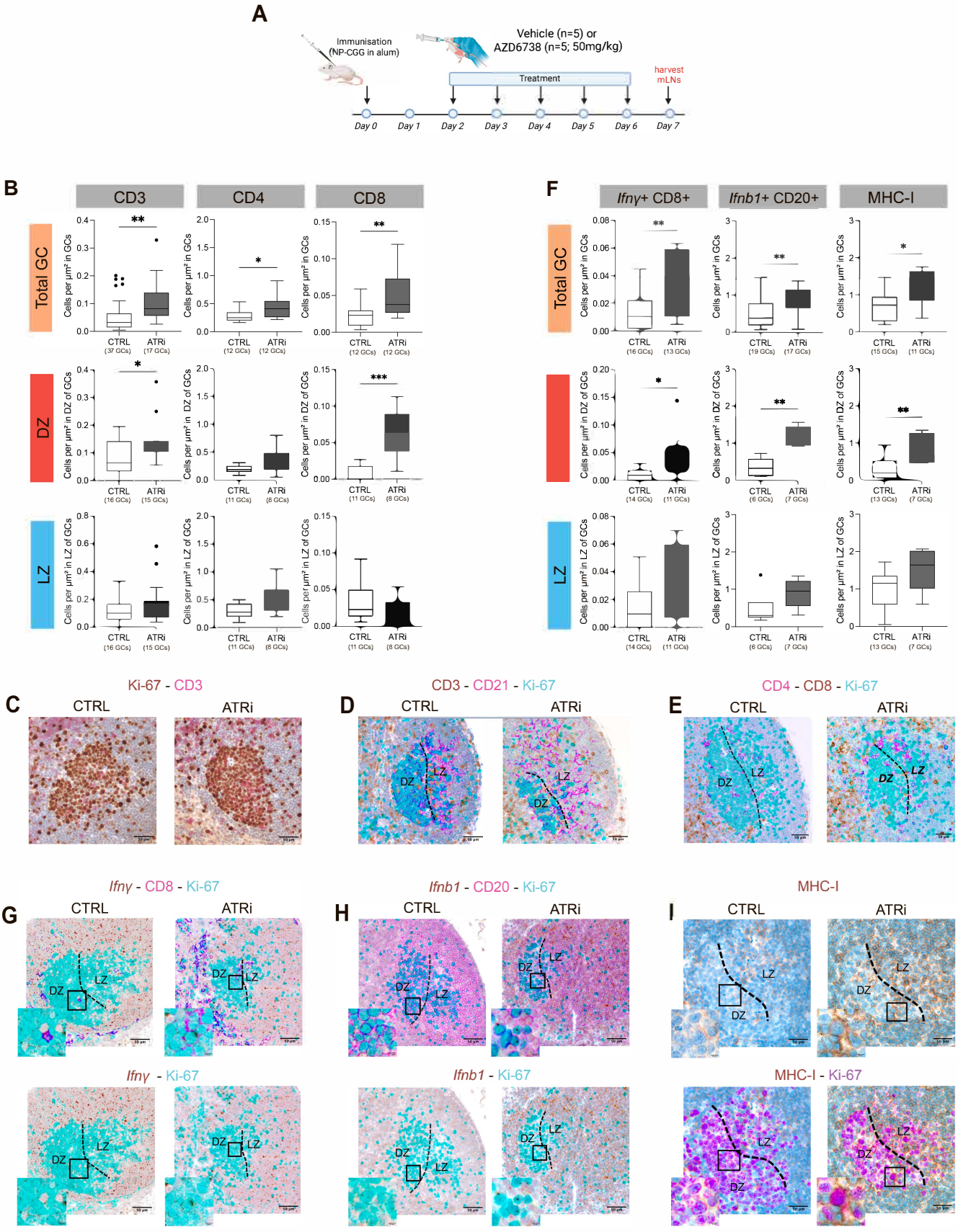
A
Immunisation (NP-CGG in alum)
Vehicle (n=5) or AZD6738 (n=5; 50mg/kg)
Treatment
harvest mLNs
Day 0
Day 1
Day 2
Day 3
Day 4
Day 5
Day 6
Day 7
B
CD3
CD4
CD8
Total GC
DZ
LZ
Cells per µm² in GCs
Cells per µm² in DZ of GCs
Cells per µm² in LZ of GCs
CTRL
ATRi
F
Ifnγ+ CD8+
Ifnb1+ CD20+
MHC-I
C
Ki-67 - CD3
D
CD3 - CD21 - Ki-67
E
CD4 - CD8 - Ki-67
G
Ifnγ - CD8 - Ki-67
Ifnγ - Ki-67
H
Ifnb1 - CD20 - Ki-67
Ifnb1 - Ki-67
I
MHC-I
MHC-I - Ki-67
DZ
LZ